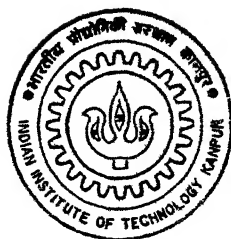# VISUALISATION OF THE OPTICAL FIELD PATTERNS IN TRANSMITTER PACKAGES

by

SATYABRATA JIT

DEPARTMENT OF ELECTRICAL ENGINEERING

INDIAN INSTITUTE OF TECHNOLOGY KANPUR

JULY, 1995

VISUALISATION OF THE OPTICAL FIELD PATTERNS IN TRANSMITTER PACKAGES

A Thesis Submitted

in Partial Fulfilment of the Requirements

for the Degree of

MASTER OF TECHNOLOGY

by

Satyabrata Jit

to the

DEPARTMENT OF ELECTRICAL ENGINEERING

INDIAN INSTITUTE OF TECHNOLOGY KANPUR

July, 1995

EE-1995-M-JIT-VIS
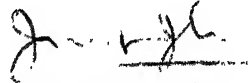
Dedicated

to

my parents

Certificate

It is certified that the work entitled VISUALISATION OF THE OPTICAL FIELD PATTERNS IN TRANSMITTER PACKAGES, by **Satyabrata Jit** has been carried out under our supervision and that this work has not been submitted elsewhere for a degree.

19 July, 1995

Dr. Anjan K. Ghosh,

Associate Professor,

Department of Electrical Engineering

IIT Kanpur.

Dr. Joseph John,

Assistant Professor,

Department of Electrical Engineering

IIT Kanpur.

Acknowledgements

I would like to express my deep sense of gratitude to Dr. Anjan K. Ghosh for his constant encouragement. Only because of his constant support, I have been able to complete this work.

I am grateful to Dr. Joseph John who helped me from time to time inspite of his busy schedule.

I would like to thank all my M.Tech batchmates for the memorable moments that we all had together. Also I would specially like to thank Tapan, Manas, Anand, Sudarshan and Santanu for helping me out of difficulties during the preparation of the thesis report and provided me mental support from time to time.

My stay here was possible due to the constant moral support provided by my family.

July 19, 1995   Satyabrata Jit.

Contents

List of Figures

Abstract

Visualisation of the optical field characteristics within the source-fiber region in transmitter packages is presented using the Finite Difference–Time Domain (FD–TD) method in two dimensional configuration. The reflection characteristics of the optical field from the fiber end face and the coupling efficiency are studied for three coupling arrangement schemes viz. centering a flat fiber end face directly over the light source; using a taper-end fiber; and placing a microsphere in between the light source and the flat fiber end face. Finally, the effect on the field pattern and the coupling efficiency due to the misalignment is studied only for the third coupling scheme.

Chapter 1

Introduction

1.1   General

The main sections of an optical fiber communication link (Figure 1.1) are a transmitter consisting of a LED or laser diode and its associated drive circuitry, an optical fiber as the transmission medium, and a receiver consisting of a photodetector plus an amplifier and

TRANSMITTER

RECEIVER
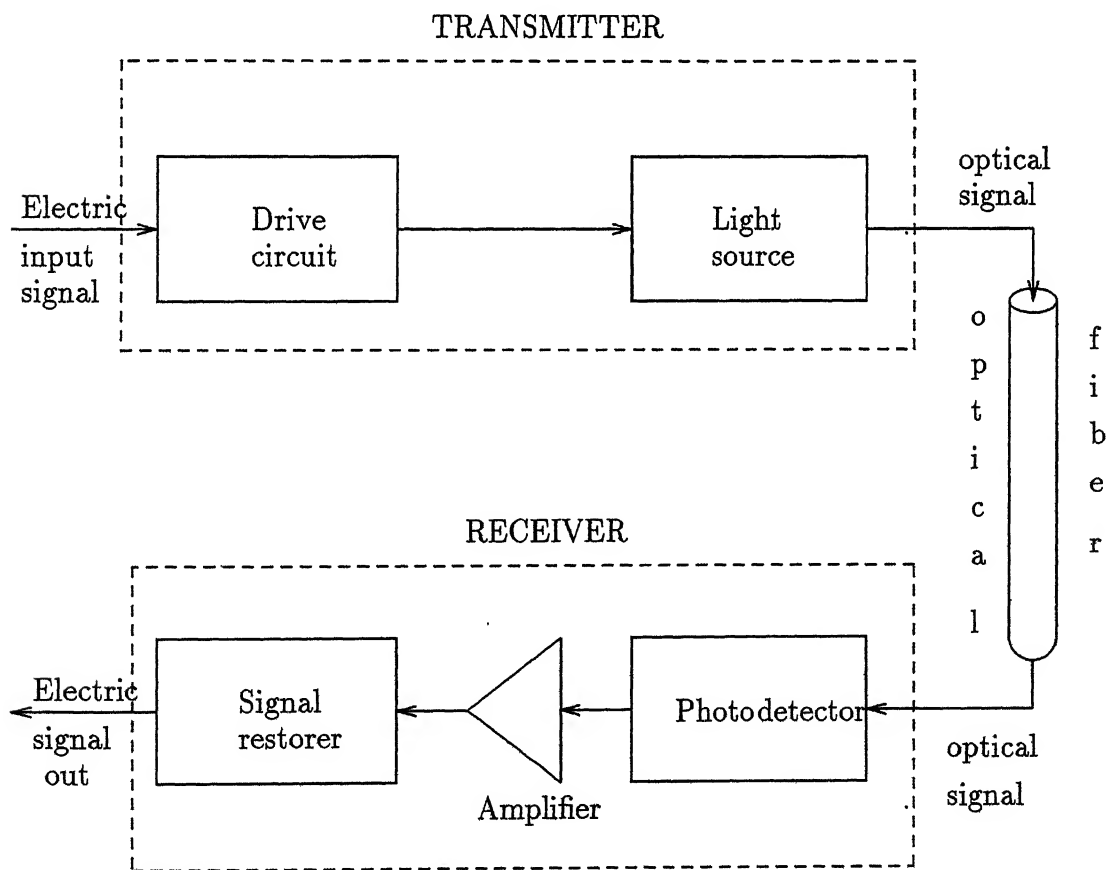
Figure 1.1: Basic configuration of an optical fiber transmission link.

signal- restoring circuitry. In the transmitter optical power is coupled from the source into the fiber.

When the source is turned on optical field propagates towards the fiber and a part of the input energy is reflected back towards the source at the air-core and air-cladding boundaries, and a part of the remaining portion of the input energy couples into the fiber and propagates. At the receiving end of fiber, power propagates towards a photodetector in the receiver which converts the optical energy into the electrical signal.

A measure of the amount of optical power emitted from a source that can be coupled into a fiber is given by the **coupling efficiency** $\eta = \frac{P_f}{P_s}$ where P_f is the power coupled into the fiber and P_s is the power emitted by the source. The more the coupling efficiency the better the performance of the communication link. The coupling efficiency depends on the optical source used, the type of fiber and on the coupling process, whether or not lenses or other coupling attachments are used.

Nowadays, people are interested in the packaging of optical systems. For a compact packaging of the optical transmitter/receiver systems, we must about the field characteristics between the optical source/detector and the coupling end of the fiber. It is also important to know about the coupling efficiency for different attaachment schemes. Visualisation of the optical field characteristics within the narrow coupling regions mentioned above is neither possible experimentally nor theoretically. The main purpose of this thesis is to visualize the optical fields in the coupling regions of transmitter packages and to throughly determine the improvements, if any, due to coupling attachments and degradations in coupling owing to misallingments.

1.2   Some Coupling Models

Several possible coupling configurations are given in Figures 1.2 to 1.9 [16, 17, 18, 19, 20, 21, 22, 23, 24, 25]. In Figure 1.2 we have shown optical power-launching based on centering a flat fiber end face directly over the light source and it is kept as close as possible to the source [29]. In this configuration, if the source emitting area is larger   than the fiber core area, then the resulting optical power coupled into the fiber is the maximum that can be achieved. In Figure 1.3 a taper-ended fiber is centered instead of the flat fiber end face [21]. In Figure 1.4
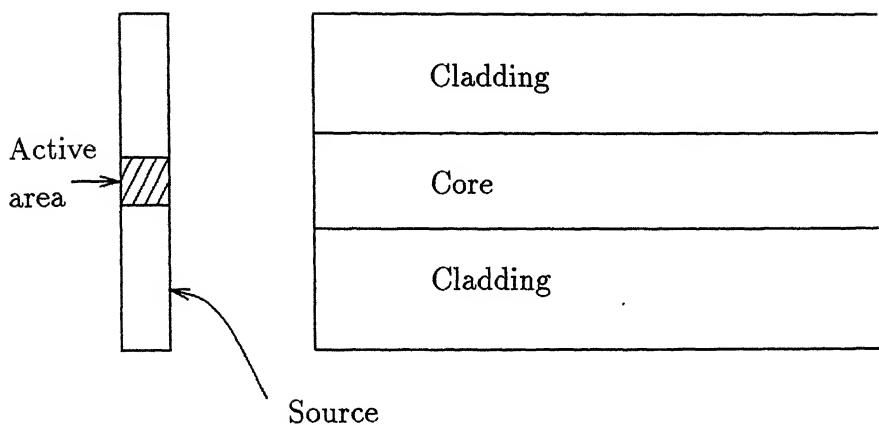
Figure 1.2: Power coupling based on centering a flat fiber end face directly over the source.
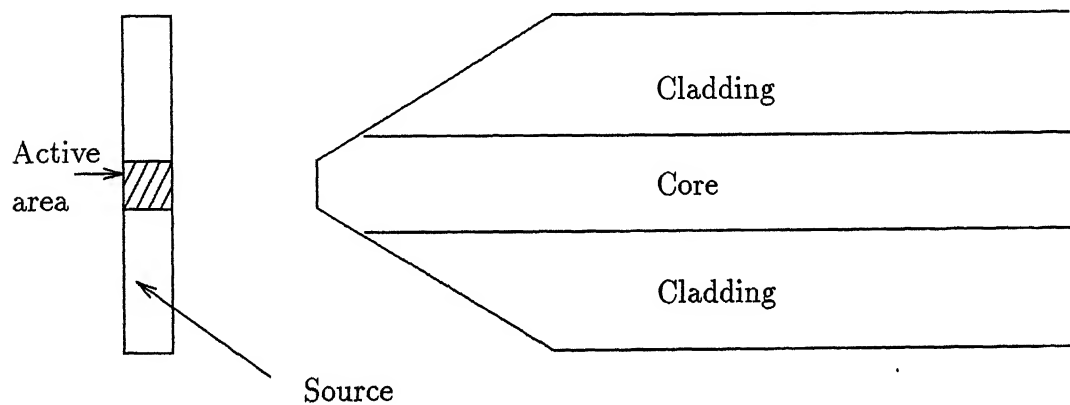
Figure 1.3: A taper-ended fiber is centered over the light source.
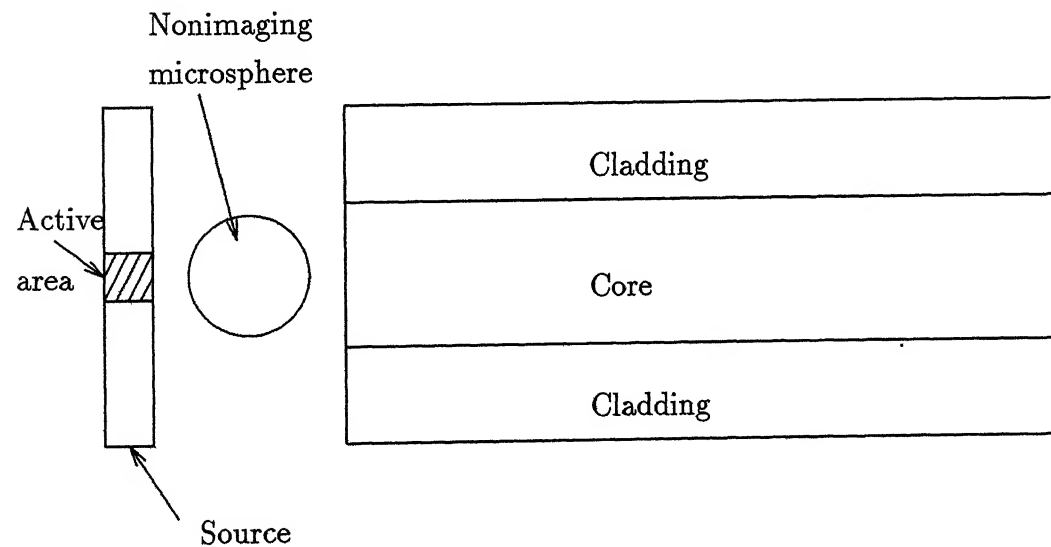
Figure 1.4: A nonimaging microsphere is placed between source and fiber end face.
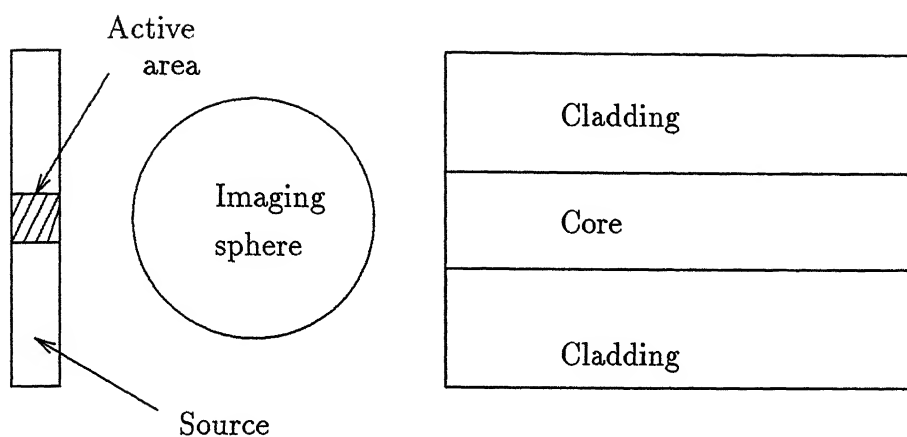
4

Active
area

Cladding

Imaging
sphere

Core

Cladding

Source

Figure 1.5: A larger spherical lens is used to image the source on the core area of the fiber end.

Gradient-index lens

Cladding

Active
area

Core

Cladding
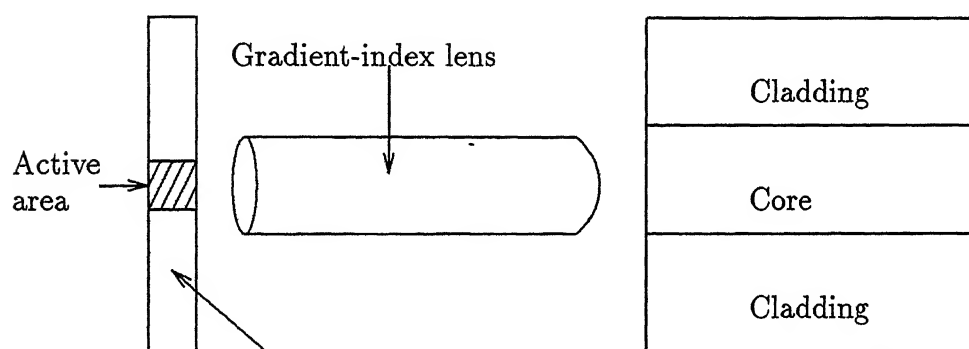
Figure 1.6: Coupling configuration using gradient-index lens.

Cladding

Active
area

Core
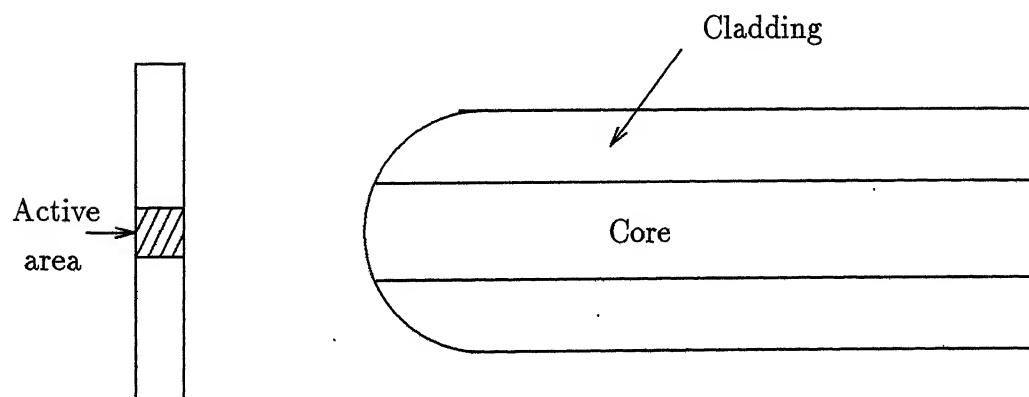
Figure 1.7: A rounded-end fiber is used in place of a flat fiber
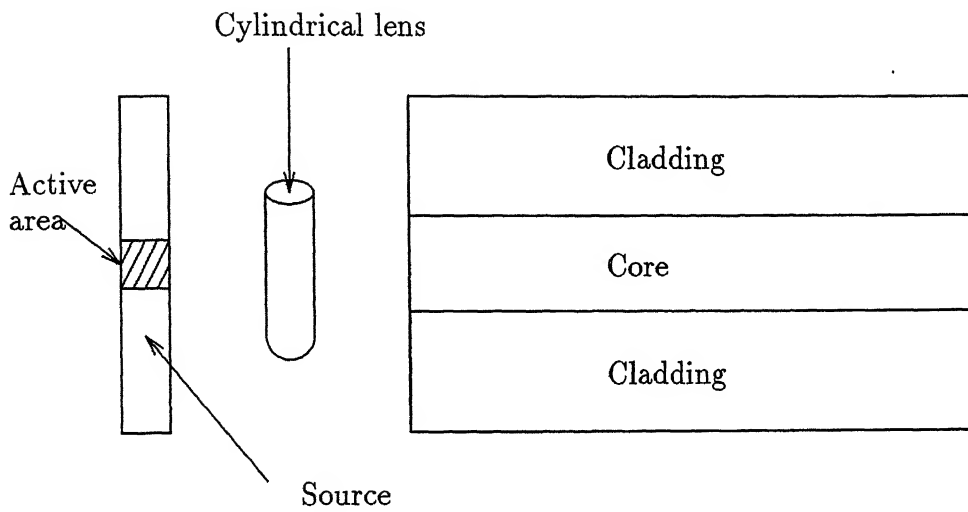
Figure 1.8: A cylindrical lens formed from a section of fiber is used in between the source and the flat fiber end.
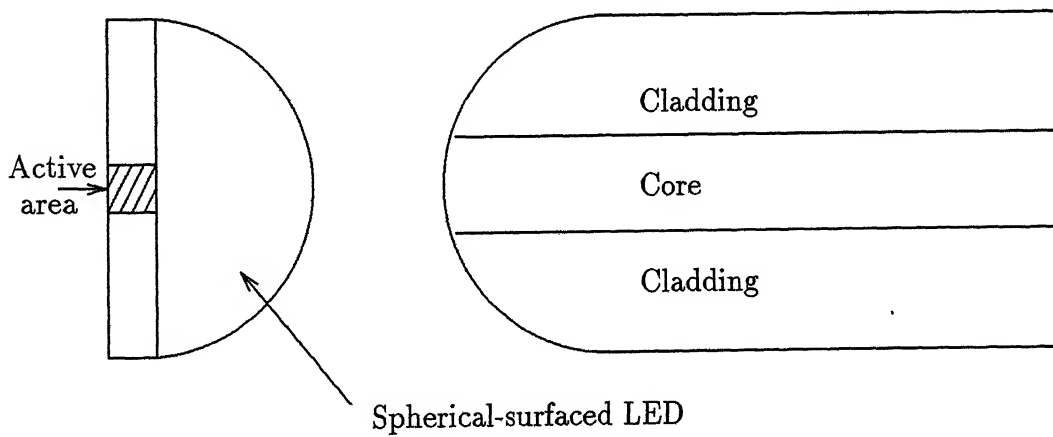
Figure 1.9: Coupling configuration consisting of a spherical-surfaced LED and spherical-ended fiber.

a nonimaging microsphere [23] is placed in between the source and the flat fiber end face. This is kept in contact with both the fiber and the source. In Figure 1.5 a larger spherical lens is used to image the source on the core area of the fiber end [20]. In Figure 1.6 we have shown the coupling configuration using graded-index lens [16, 17, 18, 19, 20]. In Figure 1.7 a rounded-end fiber is used in place of a flat fiber end face [22]. A cylindrical lens generally formed from a short section of fiber is placed in between the source and the flat fiber end face as shown in Figure 1.8 [29]. Finally, in Figure 1.9 we have presented a coupling configuration which consists of a spherical- surfaced LED and spherical-ended fiber [25].

Although these techniques can improve the coupling efficiency over the butt coupling (Figure 1.2), they also cause additional fabrication and handling difficulties. In case of taper-ended fiber the mechanical alignment must be done with greater precision since the coupling efficiency becomes a more sharply peaked function of the spatial alignment. However, alignment tolerances are increased for other types of lensing schemes [21].

Now some questions arise: what are the optical field characteristics within the regions between the source and the fiber end and how can we visualize these field characteristics for different configurations of coupling? How does the coupling efficiency change for different configurations of coupling as shown in Figures (1.2– 1.9)? How does the coupling efficiency vary due to the misalignment for the above configurations?

The first configuration (Figure 1.2) is the simplest one. The second (Figure 1.3)and third (Figure 1.4) configuratios are somehow more compliacted than the first configuration. These three configurations are very easy to implement in the computer. That is why, we consider the above three as the basic configurations to answer the above questions.

1.3   Problem Description

If we take a laser as the light source, its output intensity distribution in the transverse directions is Gaussian when it oscillates in the fundamental mode. The output of the source can be given by a set of electromagnetic field components. When the source is turned on electromagnetic waves propagate towards the fiber coupling end and are diffracted. But, the diffraction formulas available in the literature are the approximations and these are only applicable beyond a certain distance from the source. Therefore visualisation of the optical

field characteristics is not possible analytically within a small distance(in μm range). That is why we need numerical methods to visualize the above field characteristics.

In this thesis we have tried to visualize the optical field characteristics within the regions between the Source-fiber in the transmitter system using a computational technique named Finite Difference Time Domain (FD–TD) method [1, 2, 3, 4]. We have also tried to compare the coupling efficiency for three coupling models (Figure ??– ??). Though there are several methods like TLM (Transmission Line Matrix) [15], Moment method [14], Iteration method [12] etc. to solve the field problems numerically, we have used FD–TD method due to its high accuracy and ease of implementation on computers. By this method the Maxwell's equations are discretized in both space and time and then solved in time marching sequence by alternatively calculating the electric and magnetic fields in an interlaced grid. Boundary condition named absorbing boundary condition (ABC) should be applied on the boundaries of the computation domain to simulate the unbounded physical surroundings. We have used Mur's second order ABC to implement the FD–TD method [5].

To implement the FD–TD method in three dimensional configuration, it requires a large amount of computer memory as well as computation time. Therefore we have studied in the two dimensional configurations only. We have assumed that the fields do not vary in the x direction. Fiber is assumed as the planner slab wave guide with axis along the z axis. We have studied only for TE mode of propagation with field components E_x, H_y and H_z. Other field components are assumed to be zero. Our study can be easily extended to TM modes.

As the equilibrium numerical aperture of a fiber can be obtained after propagating a long distance which may be several meters (for long fibers it is taken as 50 m), an equilibrium mode can not be obtained by analyzing the FD–TD method. Therefore, the study of the coupling efficiency accurately is not possible.

We have studied only three coupling configurations given by Figures 1.2 to 1.4 for single moded step index fiber with core width $=8.4\mu m$ and cladding width$=120\mu m$(total); core refractive index$=1.50$ and cladding refractive index$=1.499$.

1.4   Overview Of The Thesis:

In chapter-2 we present a brief description of the Finite Difference–Time Domain method and Mur's absorbing boundary condition (ABC). In chapter-3 the results and discussions are given for three transmitter packages. The further scope of work is discussed in chapter-4. Finally, the conclusions are presented in chapter-5.

Chapter 2

The Finite Difference Time Domain Method

2.1 Introduction

In this chapter, we give a brief description about the Finite Difference - Time Domain (FD - TD) method [1, 2, 3, 4] and Mur's absorbing boundary condition (ABC) [5] which has been used to solve our thesis problem. The FD - TD method is a very useful method to solve Maxwell's curl equations numerically and it is a very handy computational technique for a wide variety of problems in electromagnetic radiation, scattterering and diffraction in both homogeneous and inhomogeneous media. Simulation of electromagnetic problems using the FD - TD method was first proposed by K.S.Yee in 1966 [1]. Following Yee's method Maxwell's equations are discretized both in time and space and then solved in time marching sequence by alternatively calculating the electric and magnetic fields in an interlaced grid. The resulting FD - TD method allows propagation of waves in all directions.

Many of the applications involve modeling electromagnetic fields in an unbounded space. But, due to the limited storage space of the computers, numerical computation space must be finite. Therefore, a certain kind of boundary condition, which is called the absorbing boundary condition (ABC), needs to be applied on the artificial boundaries of the computation domain to simulate the unbounded physical surroundings. Though there are several higher order ABC developed so far in the literature [6, 7, 8, 9] Mur's second order ABC is used all through this thesis to simulate the infinite physical space to a finite computation domain due to its less amount storage requirements and ease of implementation.

In section 2.2, a brief review of the derivation of the discretized form of the Maxwell's

equations is presented. In section 2.3, Mur's ABC is given in discretized form. In section 2.4, software implementation of the FD–TD method to study the propagation characteristics of a point source and some numerical results using the above ABC are presented. Finallly, section 2.5, gives some concluding remmarks and discussions.

2.2   Maxwell's Equations And The Equivalent Set Of Finite Difference Equations

The relations among the electric field vector ($\mathbf{E}$), magnetic field vector ($\mathbf{H}$), electric displacement vector ($\mathbf{D}$), magnetic flux density vector ($\mathbf{B}$) and current density vector ($\mathbf{J}$) are given by the Maxwell's equations:

$$\frac{\partial \mathbf{B}}{\partial t} + \nabla \times \mathbf{E} = 0 \tag{2.1}$$

$$\frac{\partial \mathbf{D}}{\partial t} - \nabla \times \mathbf{H} = \mathbf{J} \tag{2.2}$$

$$\nabla \cdot \mathbf{D} = \rho \tag{2.3}$$

$$\nabla \cdot \mathbf{B} = 0 \tag{2.4}$$

$$\mathbf{B} = \mu \mathbf{H} \tag{2.5}$$

$$\mathbf{D} = \epsilon \mathbf{E} \tag{2.6}$$

$$\mathbf{J} = \sigma \mathbf{E} \tag{2.7}$$

where μ, ϵ, σ, ρ are the permeability, permittivity, conductivity and charge density respectively and are assumed to be function of space and time. Assuming the medium to be charge free (i.e. $\rho = 0$) and using rectangular coordinate system, (2.1) and (2.2) can be expressed to the following set of scalar equations:

$$-\frac{\partial B_x}{\partial t} = \frac{\partial E_z}{\partial y} - \frac{\partial E_y}{\partial z} \tag{2.8}$$

$$-\frac{\partial B_y}{\partial t} = \frac{\partial E_x}{\partial z} - \frac{\partial E_z}{\partial x} \tag{2.9}$$

$$-\frac{\partial B_z}{\partial t} = \frac{\partial E_y}{\partial x} - \frac{\partial E_x}{\partial y} \tag{2.10}$$

$$\frac{\partial D_x}{\partial t} = \frac{\partial H_z}{\partial y} - \frac{\partial H_y}{\partial z} - J_x \tag{2.11}$$

$$\frac{\partial D_y}{\partial t} = \frac{\partial H_x}{\partial z} - \frac{\partial H_z}{\partial x} - J_y \tag{2.12}$$

$$\frac{\partial D_z}{\partial t} = \frac{\partial H_y}{\partial x} - \frac{\partial H_x}{\partial y} - J_z \tag{2.13}$$
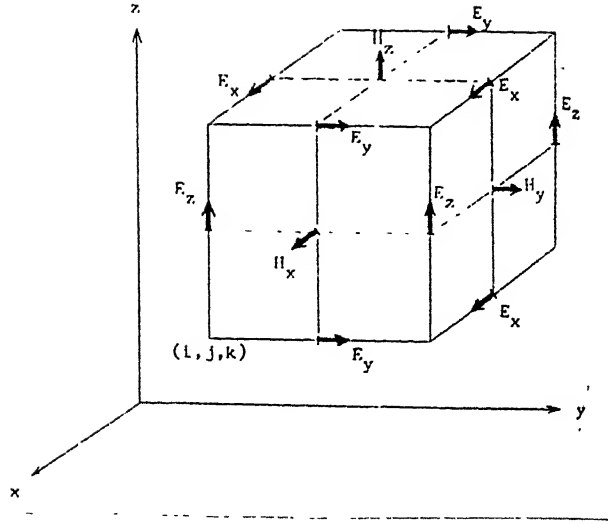
Figure 2.1: Positions of the field components about a unit cell of the Yee lattice. The E - components are in the middle of the edges and the H - components are in the center of the faces.

where the subscripts x, y and z denote the x, y and z components of **E**, **H**, **D**, **B**, and **J** vectors and each component is a function of x, y, z and t.

We denote a grid point of the space as

$$(i, j, k) \;=\; (i\delta x, j\delta y, k\delta z) \tag{2.14}$$

and for any function of space and time we put

$$F(i\delta x, j\delta y, k\delta z, n\delta t) \;=\; F^n(i, j, k) \tag{2.15}$$

Now, if we use a centered difference scheme for both space and time, eqn. (2.8) can be discretized to :

$$\frac{B_x^{n+\frac{1}{2}}(i, j + \frac{1}{2}, k + \frac{1}{2}) - B_x^{n-\frac{1}{2}}(i, j + \frac{1}{2}, k + \frac{1}{2})}{\delta t}$$
$$= \frac{E_y^n(i, j + \frac{1}{2}, k + 1) - E_y^n(i, j + \frac{1}{2}, k)}{\delta z}$$
$$- \frac{E_z^n(i, j + 1, k + \frac{1}{2}) - E_z^n(i, j, k + \frac{1}{2})}{\delta y} \tag{2.16}$$

For (2.11) we have

$$\frac{D_x^n(i+\tfrac{1}{2},j,k) - D_x^{n-1}(i+\tfrac{1}{2},j,k)}{\delta t}$$

$$= \frac{H_z^{n-\frac{1}{2}}(i+\tfrac{1}{2},j+\tfrac{1}{2},k) - H_z^{n-\frac{1}{2}}(i+\tfrac{1}{2},j-\tfrac{1}{2},k)}{\delta y}$$

$$- \frac{H_y^{n-\frac{1}{2}}(i+\tfrac{1}{2},j,k) - H_y^{n-\frac{1}{2}}(i+\tfrac{1}{2},j,k-\tfrac{1}{2})}{\delta z}$$

$$+ \quad J_x^{n-\frac{1}{2}}(i+\frac{1}{2},j,k) \tag{2.17}$$

The above discretization rule to solve the electromagnetic field comonents numerically, was first proposed by K.S.Yee and therefore it is also called the Yee's algorithm. According to this algorithm, the positions of the electric and magnetic field components can be shown as in Figure 2.1 .

Using the same discretization rule for other scaler equations in (2.8)–(2.13) and (2.3)–(2.7); rearranging the terms and considering the programming constraints, the electric and magnetic field components can be given in discretized form by the following six equations [11]:

$$E_x^{n+1}(i,j,k) = \left[1 - \frac{\sigma(i,j,k)}{\epsilon(i,j,k)}\right] E_x^n(i,j,k)$$

$$+ \quad \frac{\delta t}{\epsilon(i,j,k)} \left[\frac{H_z^{n+\frac{1}{2}}(i,j+1,k) - H_z^{n+\frac{1}{2}}(i,j,k)}{\delta y} \right.$$

$$- \quad \left. \frac{H_y^{n+\frac{1}{2}}(i,j,k+1) - H_y^{n+\frac{1}{2}}(i,j,k)}{\delta z}\right] \tag{2.18}$$

$$E_y^{n+1}(i,j,k) = \left[1 - \frac{\sigma(i,j,k}{\epsilon(i,j,k)}\right] E_y^n(i,j,k)$$

$$+ \quad \frac{\delta t}{\epsilon(i,j,k)} \left[\frac{H_x^{n+\frac{1}{2}}(i,j,k+1) - H_x^{n+\frac{1}{2}}(i,j,k)}{\delta z} \right.$$

$$- \quad \left. \frac{H_z^{n+\frac{1}{2}}(i+1,j,k) - H_x^{n+\frac{1}{2}}(i,j,k)}{\delta x}\right] \tag{2.19}$$

$$E_z^{n+1}(i,j,k) = \left[1 - \frac{\sigma(i,j,k)}{\epsilon(i,j,k)}\right] E_z^n(i,j,k)$$

$$+ \quad \frac{\delta t}{\epsilon(i,j,k)} \left[\frac{H_y^{n+\frac{1}{2}}(i+1,j,k) - H_y^{n+\frac{1}{2}}(i,j,k)}{\delta x} \right.$$

$$- \quad \left. \frac{H_x^{n+\frac{1}{2}}(i,j+1,k) - H_x^{n+\frac{1}{2}}(i,j,k)}{\delta y}\right] \tag{2.20}$$

$$H_x^{n+\frac{1}{2}}(i,j,k) = H_x^{n-\frac{1}{2}}(i,j,k) - \frac{\delta t}{\mu(i,j,k)} \left[\frac{E_z^n(i,j,k) - E_z^n(i,j-1,k)}{\delta y} \right.$$

13

$$- \frac{E_y^n(i,j,k) - E_y^n(i,j,k-1)}{\delta z} \Bigg] \tag{2.21}$$

$$H_y^{n+\frac{1}{2}}(i,j,k) = H_y^{n-\frac{1}{2}}(i,j,k) - \frac{\delta t}{\mu(i,j,k)} \Bigg[\frac{E_x^n(i,j,k) - E_x^n(i,j,k-1)}{\delta z}$$

$$- \frac{E_z^n(i,j,k) - E_z^n(i-1,j,k)}{\delta x} \Bigg] \tag{2.22}$$

$$H_z^{n+\frac{1}{2}}(i,j,k) = H_z^{n-\frac{1}{2}} - \frac{\delta t}{\mu(i,j,k)} \Bigg[\frac{E_y^n(i,j,k) - E_y^n(i-1,j,k)}{\delta x}$$

$$- \frac{E_x^n(i,j,k) - E_x^n(i,j-1,k)}{\delta y} \Bigg] \tag{2.23}$$

From the above algorithm we see that, if the components of **E** are calculated at $n\delta t$, where δt is the time step, and n is any nonnegative integer, the components of **H** are calculated at $(n + \frac{1}{2})\delta t$. For this reason, this algorithm is also called the leapfrog method.

For any finite difference scheme, a stability condition must be found which guarantees that the numerical error generated in one step of the calculation does not accumulate and grow. To ensure the stability of the above time - stepping algorithm, δt is to be chosen to satisfy the following condition:

$$v_{max}\, \delta t \le \left(\frac{1}{\delta x^2} + \frac{1}{\delta y^2} + \frac{1}{\delta z^2} \right)^{-\frac{1}{2}} \tag{2.24}$$

where v_{max} is the maximum wave phase velocity expected within the medium.

2.3 Mur's ABC

Mur's second order ABC for $x = 0$ boundary plane can be given in the form of the following differential equation:

$$\left(\left(\frac{1}{v_p} \frac{\partial^2}{\partial x\, \partial t} - \frac{1}{v_p^2} \frac{\partial^2}{\partial t^2} + \frac{1}{2} \left(\frac{\partial^2}{\partial y^2} + \frac{\partial^2}{\partial z^2} \right) \right) U \right)_{x=0} = 0 \tag{2.25}$$

where U can be any electric field component at the boundary $x = 0$ and v_p is the phase velocity of the wave in the medium. A popular discretization of 2.25 is

$$\frac{1}{v_p} D_+^x D_0^t U_{0,j,k}^n - \frac{1}{2v_p^2} D_+^t D_-^t \left(U_{0,j,k}^n + U_{1,j,k}^n \right)$$

$$+ \frac{1}{4} \Big[D_+^y D_-^y \left(U_{0,j,k}^n + U_{1,j,k}^n \right) + D_+^z D_-^z \left(U_{0,j,k}^n + U_{1,j,k}^n \right) \Big] = 0 \tag{2.26}$$

Here, D_+^q, D_-^q and D_0^q are the standard forward, backward and central difference operators and $U_{i,j,k}^n = U(i\delta x, j\delta y, k\delta z, n\delta t)$; δx, δy and δz are the grid sizes in the x, y and z directions,

respectively, and δt is the time step. The above equation (2.26) can also be given as

$$
\begin{aligned}
U_{0,j,k}^{n+1} &= -U_{1,j,k}^{n-1} + \frac{v_p \delta t - \delta}{v_p \delta t + \delta} \left(U_{1,j,k}^{n+1} + U_{0,j,k}^{n-1} \right) \\
&+ \frac{2\delta}{v_p \delta t + \delta} \left(U_{1,j,k}^{n} + U_{0,j,k}^{n} \right) + \frac{v_p^2 \delta t^2}{2\delta(v_p \delta t + delta)} \Big(U_{1,j+1,k}^{n} \\
&- 2U_{1,j,k}^{n} + U_{1,j-1,k}^{n} + U_{0,j+1,k}^{n} - 2U_{0,j,k}^{n} + U_{0,j-1,k}^{n} + U_{1,j,k+1}^{n} \\
&- 2U_{1,j,k}^{n} + U_{1,j,k-1}^{n} + U_{0,j,k+1}^{n} - 2U_{0,j,k}^{n} + U_{0,j,k-1}^{n} \Big)
\end{aligned} \tag{2.27}
$$

where we have assumed that $\delta x = \delta y = \delta z = \delta$. The boundary conditions for other planes of the artificial boundaries can be derived in the similar way as mentioned above.

For two-dimensional electromagnetic - field problems, the ABC of the second order approximation can be given in a very simple form. Suppose, the fields do not depend on z and are E - polarized, i.e., $\mathbf{E} = E_z i_z$ and $\mathbf{H} = H_x i_x + H_y i_y$. Now, (2.25) applies to E_z only and in this case we have

$$
\mu \frac{\delta H_x}{\delta t} = -\frac{\delta E_z}{\delta y} \tag{2.28}
$$

Substituting (2.28) in (2.25), putting $\delta E_z / \delta z = 0$, with $U = E_z$, integrating with respect to t and using $E_z = 0$ for $t < 0$ we get

$$
\left(\frac{\delta E_z}{\delta x} - \frac{1}{v_p} \frac{\delta E_z}{\delta t} - \frac{\mu v_p}{2} \frac{\delta H_x}{\delta y} \right)_{x=0} = 0 \tag{2.29}
$$

The discretized form of (2.29) can be given as follows:

$$
\begin{aligned}
E_z^{n+1}(0,j) &= E_z^{n}(1,j) + \frac{v_p \delta t - \delta}{v_p \delta t + \delta} \left(E_z^{n+1}(1,j) - E_z^{n}(0,j) \right) \\
&- \frac{\mu v_p^2 \delta t}{2(v_p \delta t + \delta)} \left(H_x^{n+\frac{1}{2}}(0,j+1) - H_x^{n+\frac{1}{2}}(0,j) \right. \\
&+ \left. H_x^{n+\frac{1}{2}}(1,j+1) - H_x^{n+\frac{1}{2}}(1,j) \right)
\end{aligned} \tag{2.30}
$$

We see that (2.29) is much simpler than (2.25) but still of the same order of approximation. A similar ABC for the case of H - polarization can easily be derived.

2.4 Software Implementation Of The FD–TD method: Studying With A Point Source

In this section we give the program outline for the FD–TD method to study the field characteristics of a point source in two dimensional configuration and for an isotropic, homogeneous,

source-free and nonmagnetic medium (i.e. air) in the y-z plane. The whole program can be given by the following steps.

1. Begin:
   - INPUT PARAMETERS:

2. READ: number of nodes in y-direction (y_{max}), number of nodes in z-direction (z_{max}), operating wavelength (λ), dielectric constant of the medium (ϵ) and permeability of the medium (μ_0).
   - SELECTION OF SOME PARAMETERS FOR THE FD-TD METHOD:

3. Calculate: phase velocity in the medium $(v_p) = \frac{1}{\sqrt{\mu\epsilon}}$.

4. Select: $\delta y = \delta z = \delta = \frac{\lambda}{10}$ and $\delta t = \frac{\delta}{2\,v_p}$.

5. Set the initial values of all the field components equal to zero.

6. Select: number of time steps $(n_{max}) \geq max < 2\,y_{max}, 2\,z_{max} >$

7. Select $\epsilon(j,k) = \epsilon$ for all values of j and k in the computation domain.
   - STARTING OF THE CALCULATION OF THE FIELD COMPONENTS:

8. Start time stepping (n) at $n = 0$

9. Choose a point (j_0, k_0) (say). Apply the input at this point as given by the equation (2.36).
   - CALCULATION OF THE FIELD COMPONENTS AT THE INTERRIOR NODES:

10. Calculate the field components at the interrior nodes of the computation domain with the regular finite difference scheme.
    - SPECIAL TREATMENTS OF THE BOUNDARY NODES

11. Apply Mur's second order boundary condition to calculate the electric field components at the boundary nodes of the computation domain.

12. Increase n by one i.e. $n \to n + 1$.

13. Verify: if $n \leq n_{max}$ then go to step (8); else finish.

```
                    ┌─────────────┐
                    │    Start    │
                    └──────┬──────┘
                           │
                           ▼
          ┌────────────────────────────────┐
          │     Read the input parameters  │
          └────────────────┬───────────────┘
                           │
                           ▼
          ┌────────────────────────────────┐
          │     Select the parameters      │
          │     for the FD-TD method       │
          └────────────────┬───────────────┘
                           │
                           ▼
          ┌────────────────────────────────┐◄──────────────────┐
          │     Do n=0, $n_{max}$          │                   │
          └────────────────┬───────────────┘                   │
                           │                                    │
                           ▼                                    │
          ┌────────────────────────────────┐                   │
          │     Choose a node and          │                   │
          │     apply input here           │                   │
          └────────────────┬───────────────┘                   │
                           │                                    │
                           ▼                                    │
                     ╱─────────────╲         Yes    ┌──────────────────────┐
                    ╱  Select        ╲──────────────►│  Use ABC to calculate │
                   ╱ any arbitrary node╲             │  the electric field   │
                   ╲ Is the node on the╱             │  components on the     │
                    ╲  boundary       ╱              │  boundary nodes        │
                     ╲     ?        ╱                └───────────┬──────────┘
                      ╲───┬────╱                                 │
                          │ No                                   │
                          ▼                                      │
     ┌────────────────────────────────────┐                     │
     │  Calculate the field components     │                     │
     │  using regular finite difference    │                     │
     │  scheme                             │                     │
     └────────────────┬───────────────────┘                     │
                      │◄───────────────────────────────────────┘
                      ▼
                ╱─────────────╲          Yes
               ╱     Is         ╲──────────────────────────────────┐
              ╱  $n \leq n_{max}$╲                                  │
               ╲     ?          ╱                                   │
                ╲───┬────╱                                          │
                    │ No                                            │
                    ▼                                   (to Do n=0 box)
             ┌─────────────┐
             │    Stop     │
             └─────────────┘
```
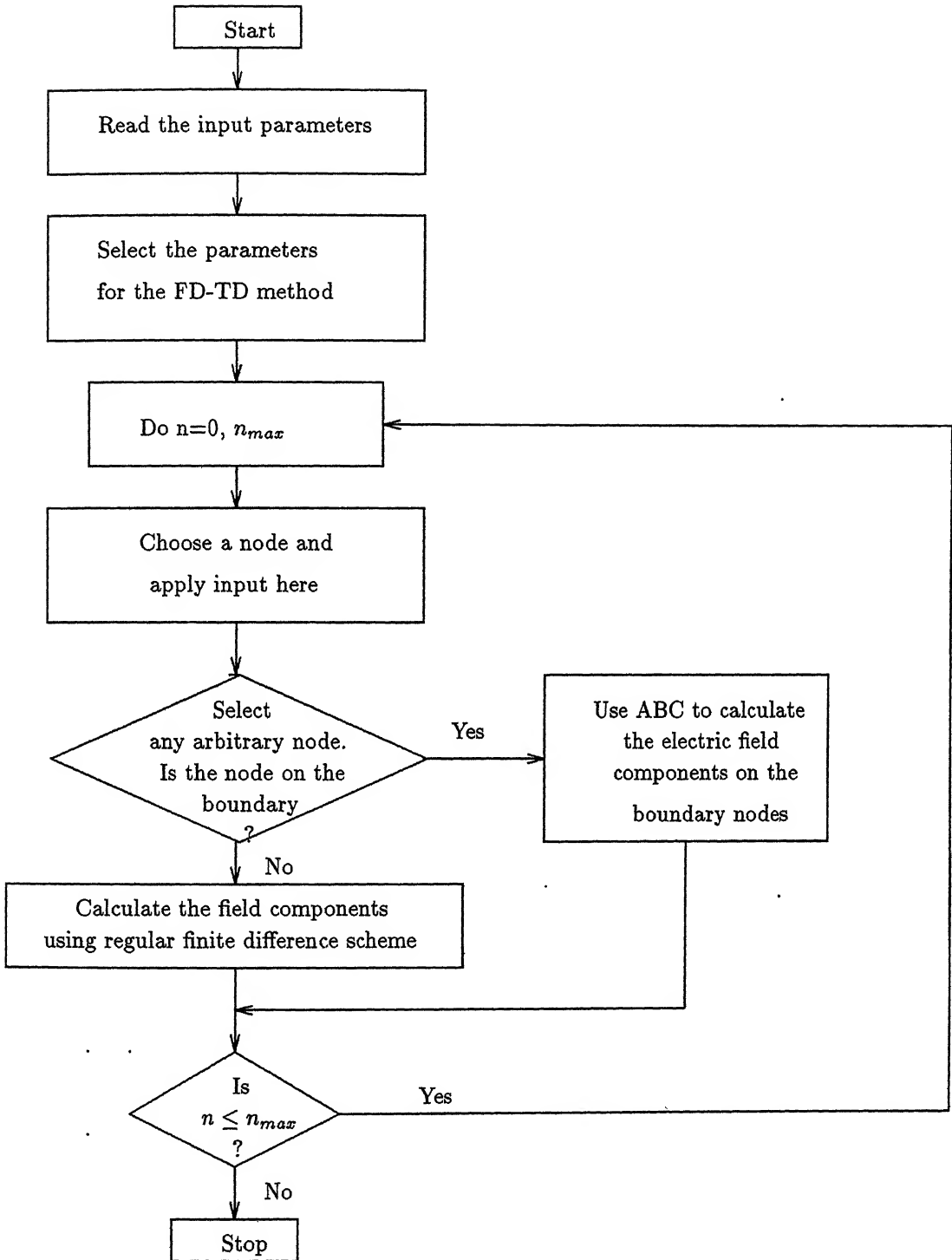
Figure 2.2: Flow chart for studying with a point source by the FD–TD method

17

14. Print outputs

15. End

The steps are shown in the flowchart (Figure 2.2)

2.4.1 Numerical Results

In this section numerical simulation is performed to test the accuracy of the ABC considered in the previous sections. We shall present results for two - dimensional configurations only. We present results for fields that do not depend on x and are TE modes i.e., $\mathbf{E} = E_x i_x$ and $\mathbf{H} = H_y i_y + H_z i_z$; where i_x, i_y and i_z are the unit vectors along the x, y and z directions, respectively. A square two - dimensional mesh is used in the y–z plane with a size 76 by 76 i.e., $0 \leq j \leq 76$ and $0 \leq k \leq 76$. Absorbing boundary conditions are applied on all four sides of the mesh. A monochromatic isotropic point source of wavelength λ=1.5μm is assumed to be turned on at t=0 in air and $\delta = \delta y = \delta z = 2c_0 \delta t = \frac{\lambda}{10}$, where c_0 is the velocity of light in free space. Actually,the value of δy, δz and δt should be such that the following conditions [7]

$$k_y \delta y \ll 1 \tag{2.31}$$

$$k_z \delta z \ll 1 \tag{2.32}$$

$$\omega \delta t \ll 1 \tag{2.33}$$

are satisfied; where k_y and k_z are the wave numbers in the y and z directions respectively. If we assume $k_y = k_z = \frac{2\pi}{\lambda}$ and for $\delta y = \delta z = \delta$, the value of δ must have to satisfy the following condition

$$\begin{aligned} \delta \quad &<< \quad \frac{\lambda}{2\pi} \\ &= \quad \frac{\lambda}{6.28} \end{aligned} \tag{2.34}$$

That is why we have selected $\delta = \frac{\lambda}{10}$ for the FD–TD method. δt is then chosen from the stability condition given by (2.22).

An isotropic point source in two - dimensional case has a circular radiation pattern. We investigate how well this pattern is maintained on the truncated mesh by using the Mur's second order ABC. Figure 2.2 gives a clear view of the radiation pattern of the isotropic point source for two - dimensional case. It consists of the surface plot along with the contour plot
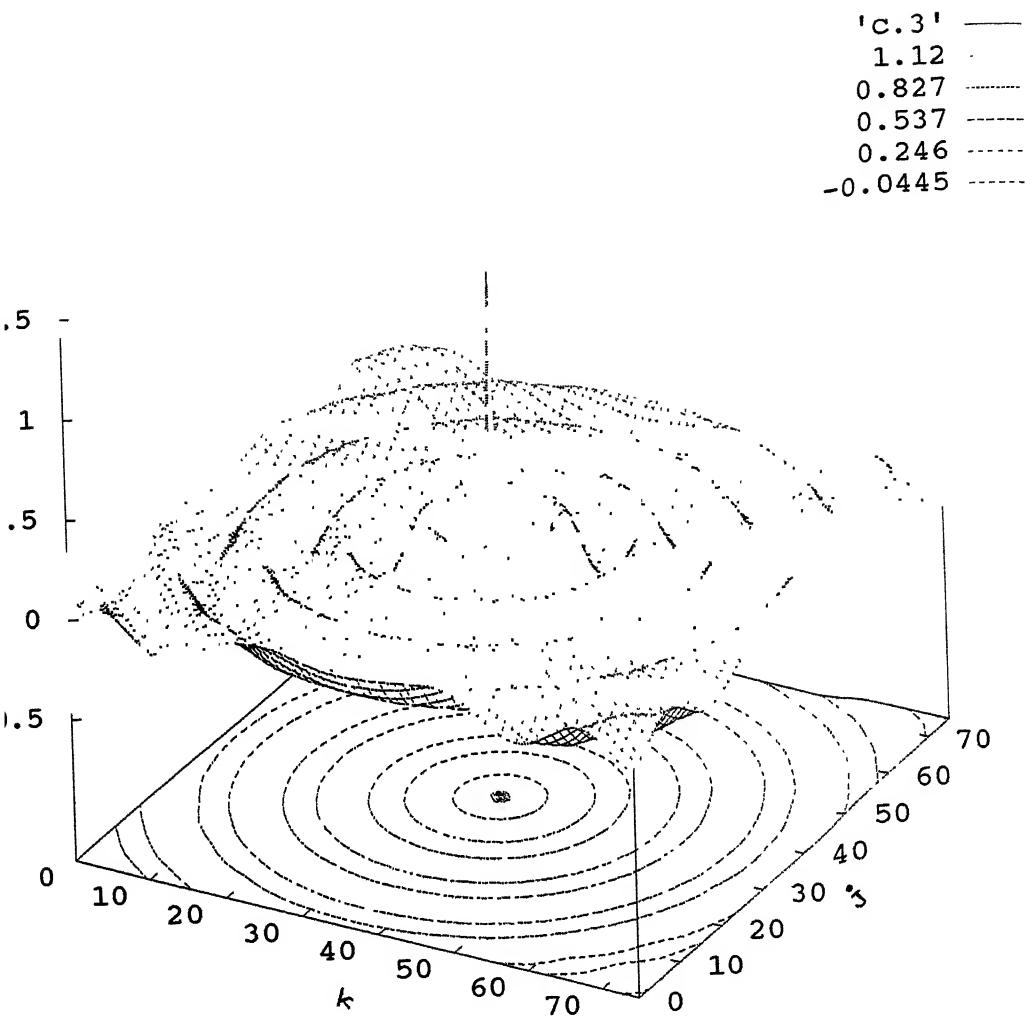
Figure 2.3: Radiation pattern of an isotropic point source: mesh size = 76 by 76, r_s=(36, 36), no. of time steps = 650; surface plot and contour plot.
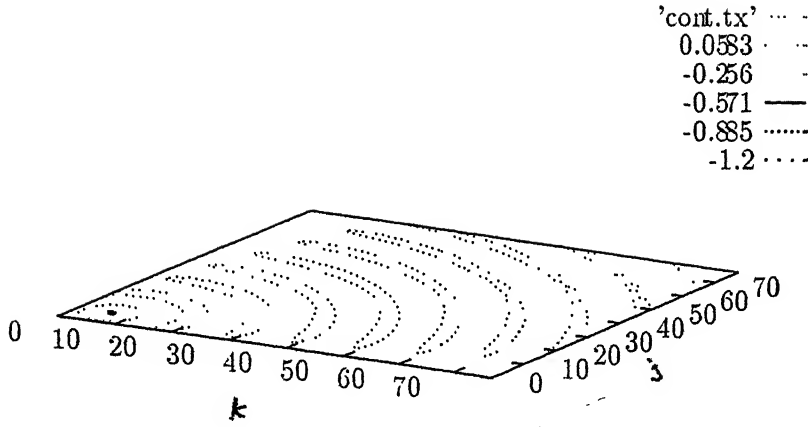
Figure 2.4: Contour plot of the radiation pattern after 650 time steps of an isotropic point source located at node (6,6) of a 76 by 76 node mesh.

[1]also. The point source is located at node (36,36) and we present the result after 650 time steps. Though the number of time steps required to propagate the field to the boundary is only 80, we select 650 to show the effect of the reflection error introduced by this ABC. The error generated in one time step of the calculation accumulate and grow during the successive time steps. From the contour plot we see that the radiation pattern is almost circular with only slight deformations at the points near the boundaries and far away from the source. These errors are caused by the fact that waves with grazing incidence on a boundary are not well absorbed, but partly (i.e. 10–15% depending on the distance from the source to the boundary) reflected. In Figure 2.4 we present the contour plot of the same dimensions except the source is located at the node (6,6). We see from the contour plot that now the patterns are not so circular as before and more deformations are introduced specially at the points far away from the source. That is why, it can be concluded that, to get more accurate results one should locate the source as far away from the boundary as possible. Since, (2.30) is very easy to implement and it gives exactly the same results as the more complicated one that follows from (2.27), we have used (2.30) for two - dimensional field problems.

---

[1]If we cut the surface plot of a function of two variables by a plane parallel to the lower plane (i.e. horizontal plane) then the variation of the function on this plane is called the contour plot

Suppose, the point source is located at $r_s = (y_s, z_s) = (j_0\delta, k_0\delta)$. Now, this point source can be modeled by adding a term representing a current [5]

$$I_x(t) = C\,sin(\frac{2\pi c_0 t}{\lambda})u(t) \tag{2.35}$$

at r_s, where $u(t)$ denotes the Heaviside unit-step function and C is a constant. That is, the input condition can be given by the following equation:

$$E_x^{n+1}(j_0, k_0) = E_x^n(j_0, k_0) + I_x(t) \tag{2.36}$$

The above equation represents the isotropic point source at the node (j_0, k_0) in the FD–TD method and C represents the amplitude of the electric field.

2.4.2 Computed Results vs Theoretical Results

Now, we will compare our computed results with the theoretical one. For the point source under consideration, the theoretical radiated field can be obtained by solving the equation:

$$\left(\frac{\partial^2}{\partial y^2} + \frac{\partial^2}{\partial z^2} - \frac{1}{c_0^2}\frac{\partial^2}{\partial t^2}\right)E_x = \mu_0\frac{\partial}{\partial t}I_x(t)\delta(r - r_s) \tag{2.37}$$

which is rotationally symmetric around r_s and consists of the outgoing waves. The solution for the electric field distribution can be given as [10]

$$E_x(r,t) = -\left(\frac{\mu_0}{2\pi}\right)\int_0^\infty \frac{\partial}{\partial t}I_x\left(t - \left(\mid r - r_s \mid^2 + \xi^2\right)^{\frac{1}{2}}/c_0\right)$$
$$\cdot \times \left(\mid r - r_s \mid^2 + \xi^2\right)^{-\frac{1}{2}}d\xi \tag{2.38}$$

The above equation can be given in the following simplified form:

$$E_x(r,t) = -\left(\frac{C\mu_0\,c_0}{\lambda}\right)\int_0^{\xi_1}\cos\left(t - \left(\mid r - r_s \mid^2 + \xi^2\right)^{\frac{1}{2}}/c_0\right)$$
$$\times \left(\mid r - r_s \mid^2 + \xi^2\right)^{-\frac{1}{2}}d\xi \tag{2.39}$$

where $\xi_1 = \sqrt{c_0^2\,t^2 - \mid r - r_s \mid^2}$. Equation (2.39) can not be put into a simple analytical formula. That is why, (2.39) is solved numerically using Simpson's rule to get the theoretical value[2] and the exact solution is plotted as a function of distance from the point source and

---

[2]This is not the exact theoretical value because a very small amount of error is introduced by the Simpson's rule. We have used Simpson's 1/3 rule to solve the equation (2.39) and the error introduced by this method is given by $E_r = \frac{\xi_1^5}{180\,m^4}f^{iv}$ where m is the number of iteration and f^{iv} is the average fourth order derivative of the function which is integrated for the interval $[0, \xi_1]$. For our case $t = 650\ \delta t$ and $m = 800$; and the maximum error introduced by the Simpson's rule is in the order of 10^{-7}–10^{-4}. This error is negligible and thererefore the results obtained by the Simpson's rule can be considered as the theoretical value.
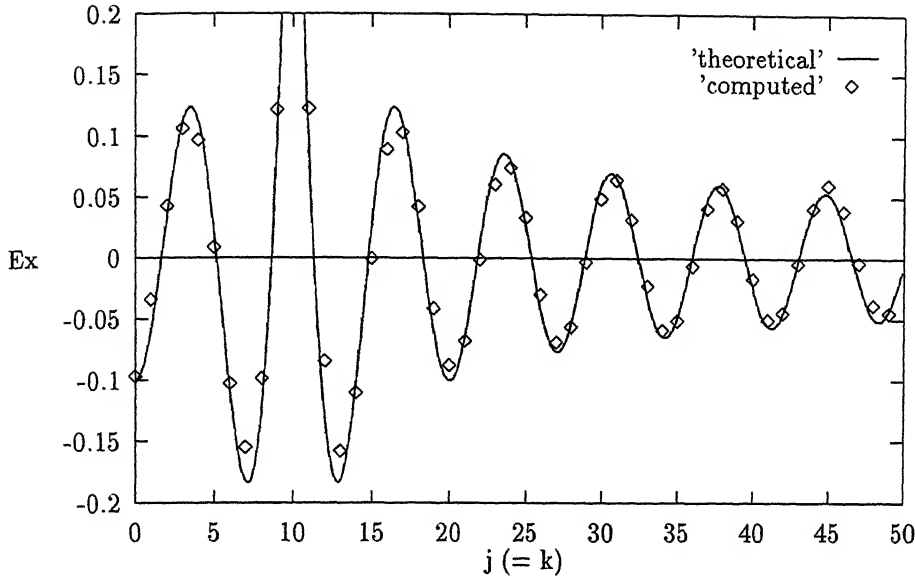
Figure 2.5: Comparison of the theoretical results and computed results. Source is located at the node $(10, 10)$. Results are compared for $j = k$ nodes.

at the same instant in time in Figure 2.5 . The results are compared for the diagonal nodes of the mesh(i.e. for $j = k$) that passes through the location of the point source. Point source is located at $(10, 10)$ and no. of time steps $= 650$. From the Figure 2.4 we see that, computed results are very similar to the theoretical one and the error introduced is very less. A maximum 15 percent error is there which may be tolerated in some of the cases.

2.5 Conclusion

In this chapter we have given a brief review of the FD–TD method and the Mur's second order ABC. We have studied the results using a point source only. We have also compared the FD–TD computed results for a point source problem with a more exact computanional result. In the next chapter we shall apply the FD–TD method for studying three coupling models as mentioned in the first chapter.

Chapter 3

Visualizing Optical Fields In Transmitter Packages

In this chapter we present numerical results about the optical field characteristics within the region between the source and the coupling end of the optical fiber for three coupling configurations. Since we are computing fields in a two dimensional domain, we approximate the fiber by a planar dielectric slab waveguide (Figure 3.1) for all the configurations under our consideration. This is composed of a dielectric slab of refractive index n_1 (=1.5) sandwiched between dielectric material of refractive index n_2 (=1.499)$\angle n_1$, which we shall call a cladding. This represents the simplest form of the optical waveguide and can serve as a model to gain an understanding of wave propagation in optical fibers in a two dimensional domain.

In the first configuration we consider a simple coupling model in which power is directly coupled into the waveguide — we call it as arrangement −1. In the second configuration we consider a different type of coupling model in which power is coupled from the source into a taper-ended optical waveguide — we call it as arrangement−2. Finally, we consider a model in which power is coupled from the source through a microsphere into the optical waveguide — we call it as arrangement −3. Before studying the different coupling configurations mentioned above we first study the propagation characteristics of a Gaussian beam in free space. We present results for two dimensional configurations using the FD–TD method and Mur's second order ABC as before. A (top emitting semiconductor) laser is used as the optical source of wavelength $\lambda = 1.5 \mu m$ and in two dimensional configuration it is assumed as a line source. We present results for y-z plane; source is assumed along the y-axis at $z = 0$ and only the TE mode is considered as in chapter 2. For all the cases, the spot size of the laser beam
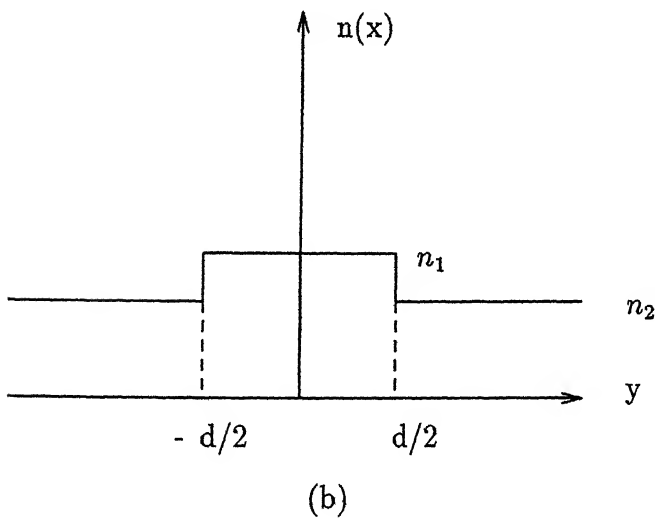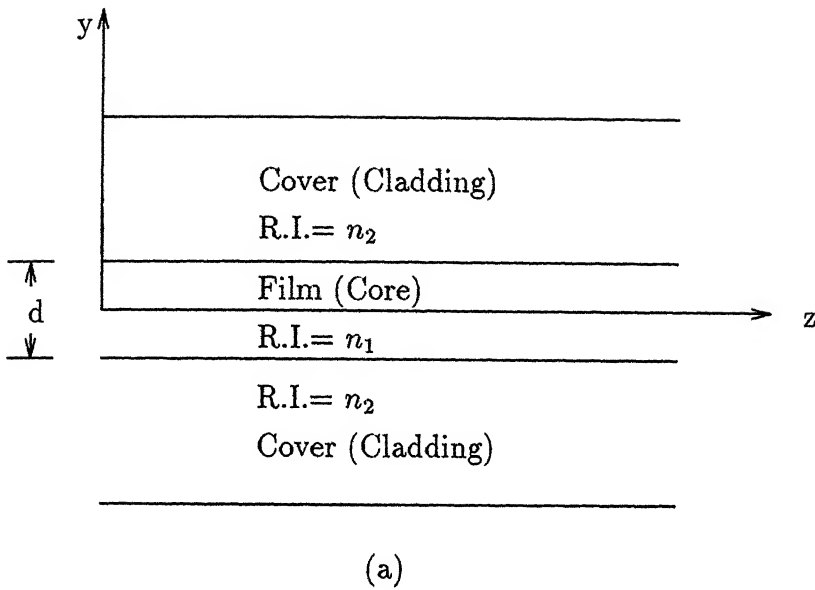
Cover (Cladding)

R.I.= n_2

Film (Core)

R.I.= n_1

R.I.= n_2

Cover (Cladding)

(a)

(b)

Figure 3.1: (a) A planar waveguide (b) Refractive index profile for the waveguide.

$\omega_0 = 3.5\mu m.$

3.1   Diffraction Of A Gaussian Beam In Air

Lasers emit Gaussian beams. In this section we present the study of the propagation of a Gaussian beam over a few micron distance away from the source in free space using the FD–TD method in two dimensional configuration. We assume only three field components; i.e. $E_x(y, z, t)$, $H_y(y, z, t)$ and $H_z(y, z, t)$. At $t = 0$, the laser source of frequency f is assumed to be turned on. The diffraction of waves from this source is modeled by solving the finite-difference analog of the time-dependent Maxwell's equations (i.e. 2.16, 2.20 and 2.21) of chapter -2.

The software outline is almost the same as given in section (2.4) of chapter 2 except the source condition. In this case the laser is assumed to be a line source along y axis and located at $k = 10$. Then the source condition for the FD–TD method can be given as follows [4]:

$$E_x^{n+1}(j, 10) = E_x^n(j, 10) + C \exp\left[-\frac{(j\ \delta y)^2}{\omega_0^2}\right] \sin(n\ \omega\ \delta t) \qquad (3.1)$$

where C is a constant and $\omega = 2\ \pi\ c_0/\lambda$. At each point on the line, the computer first calculates $E_x^n(j, 10)$ in the normal manner of the algorithm and stores the value in memory. Then the value of the sinusoidal term is calculated and added to the stored value of $E_x^n(j, 10)$. In effect, equation(3.1) simulates the linear superposition of z directed plane wave and the ambient field along the grid line $k = 10$. Equation(3.1) generates the desired sinusoidal incident plane wave. Note that, this source condition (i.e. eqn. (3.1) is also used for all models under our consideration.

The field envelope, or the maximum absolute value, during the final half-cycle of time stepping is taken as the magnitude of phasor of the steady-state field field [4]. The intensity of the electric field [1] for the different values of z is plotted in Figure 3.2. From Figure 3.2 we see that, with the increase in z, the width of the beam is also increased; and it supports the theory of diffraction of a Gaussian beam in free space. In Figure 3.3, we have plotted the error plots for the above field intensity plots. In this figure, the computed results are

---

[1]First, the absolute value of the electric field at each point in the computation domain is computed by the FD–TD method. This represents the mod of the electric field (i.e. $|E|$). Now, intensity (I) is given by the relation $I = EE^* = |E|^2$. Therefore, the square of the envelope gives the intensity of the electric field.
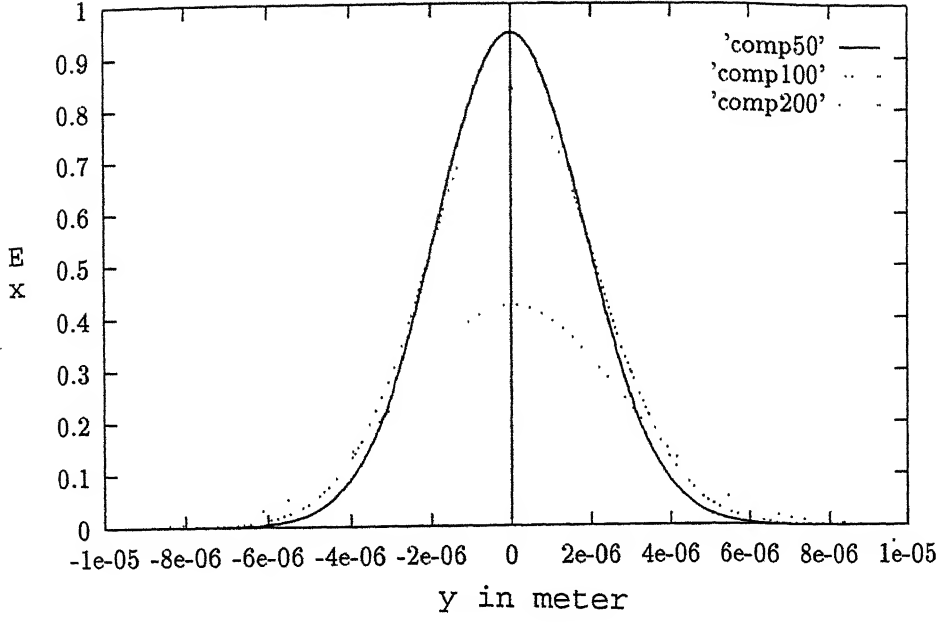
Figure 3.2: Envelopes of the electric field for different values of z: comp50 for $z = 5\lambda$, comp100 for $z = 10\lambda$ and comp200 for $z = 20\lambda$; $\lambda = 1.5\mu m$.

compared with the Fresnel diffraction formula [27]:

$$E_x(y,z) = \frac{j\, 2C\pi\, \omega_0^2}{\lambda(2z + j\, k\, \omega_0^2)} \exp\left\{-j\, k\left[z + \frac{y^2}{2z\left(1 + \pi^2\omega_0^4/\lambda^2 z^2\right)}\right]\right\}$$

$$\times \quad \exp\left[-\frac{y^2}{\omega(z)^2}\right] \tag{3.2}$$

where C is a constant and

$$\omega(z)^2 = \omega_0^2\left(1 + \frac{\lambda^2 z^2}{\pi^2\omega_0^4}\right) \tag{3.3}$$

and $k = \frac{2\pi}{\lambda}$. The intensity distribution can be given as

$$I(y,z) = A\,\exp\left[-\frac{2y^2}{\omega(z)^2}\right] \tag{3.4}$$

where

$$A = \frac{4\,C^2\pi^2\omega_0^4}{\lambda^2\left(4z^2 + k^2\omega_0^4\right)} \tag{3.5}$$

which shows that the transverse intensity distribution remains Gaussian with the beam-width increasing with z which implies diffraction divergence. ω_0 is called the spot-size of the beam.

This formula has less accuracy for small distaces from the source. That is why we see from the Figure 3.3, large amount of errors are introduced for small distances from the source and
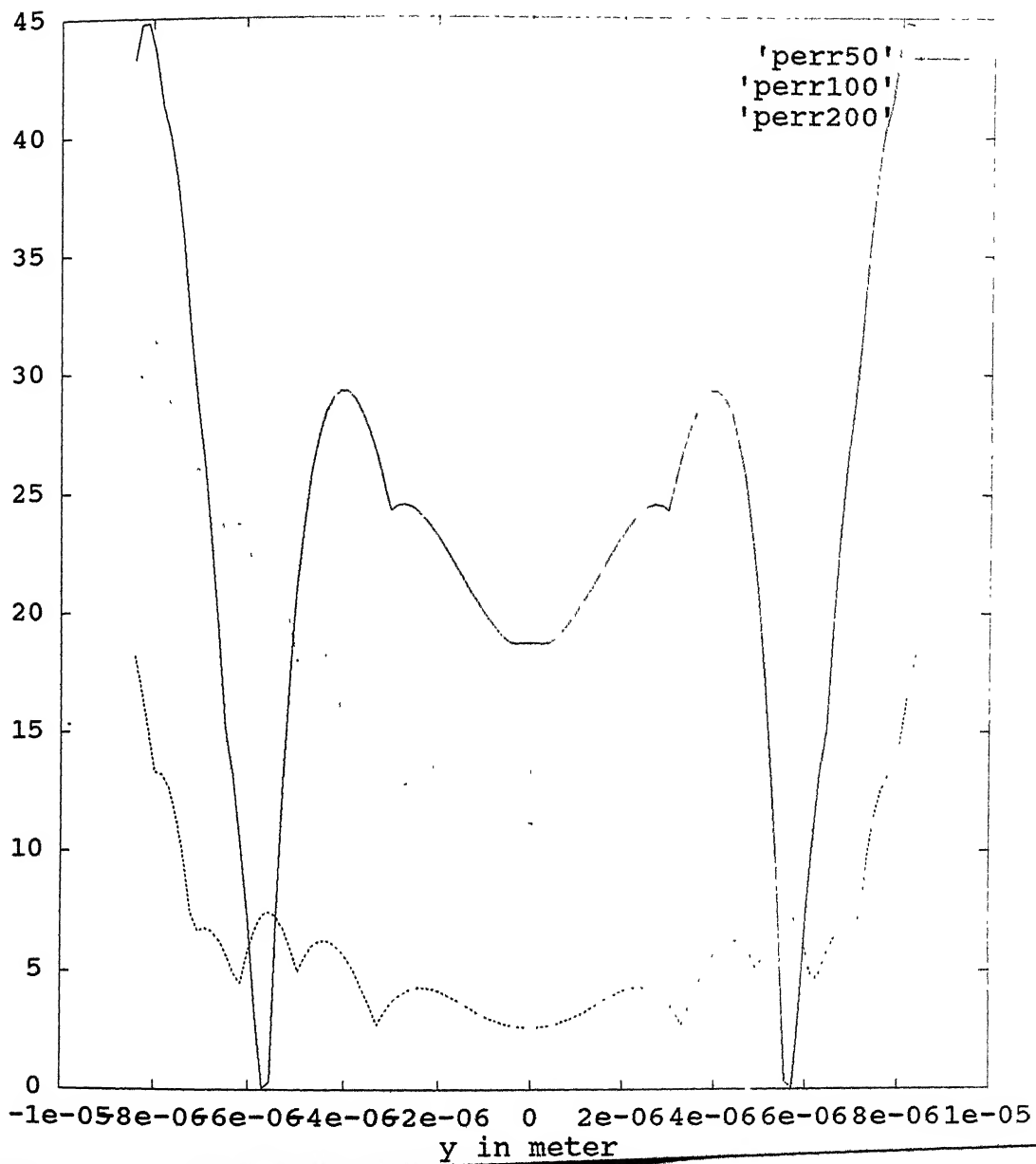
Figure 3.3: Error plots for the Gaussian beam propagation in air. perr50 is for the electric field
$Z = 5\lambda$ distance from the source, perr100 for $Z = 10\lambda$ and perr200 for $Z = 20\lambda$ distan
from the source, respectively.
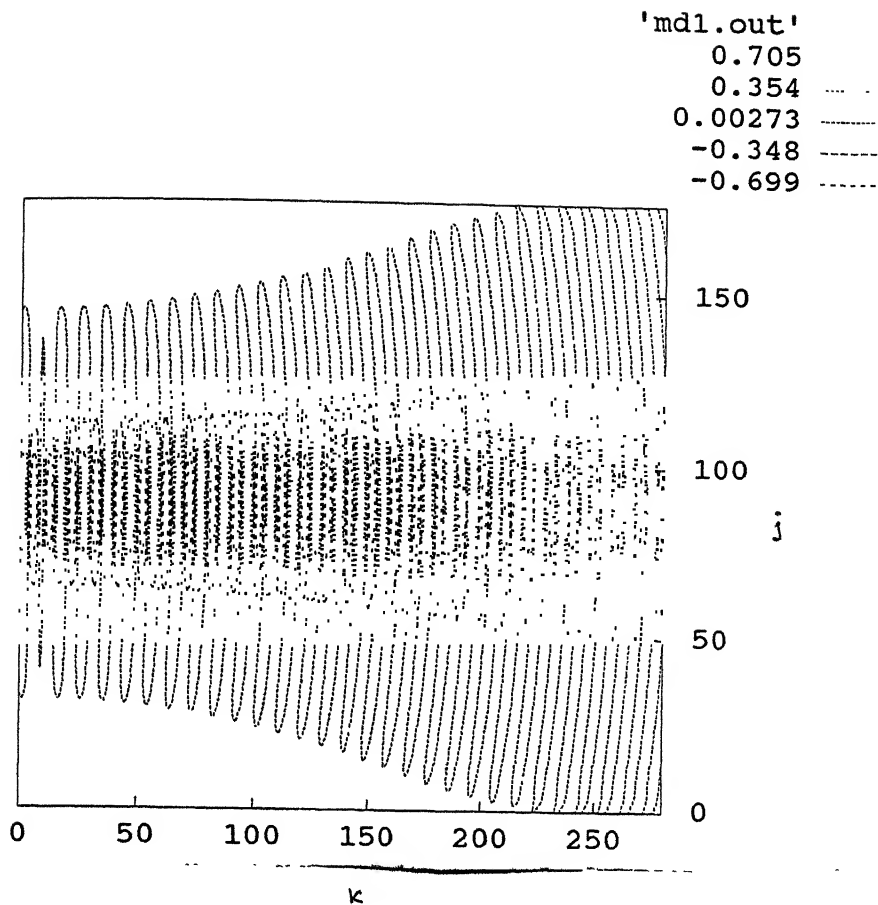
Figure 3.4: Contour plot of the electric field for Gaussian beam propagation in free space.

as the distance is increased error is reduced. In Figure 3.4, we have also given the contour plot of the electric field. From this figure we also see that, the width of the beam is increased with the increase in distance from the source and it agrees with the theoretical nature of the electric field.

3.2   Study Of Model–1

In this section we study a simple coupling model in which optical power from the source is directly coupled into the fiber (Figure 3.5). Fiber is considered as a planner wave guide in y–z plane. The fiber under consideration is assumed to be a single mode step index fiber with core width $= 8.4\mu m$ and cladding width $= 60\mu$ as mentioned in the figure. The distance between the source and the coupling end of the waveguide is assumed as $45\mu m$ and the length of the waveguide is taken as $167\mu m$.
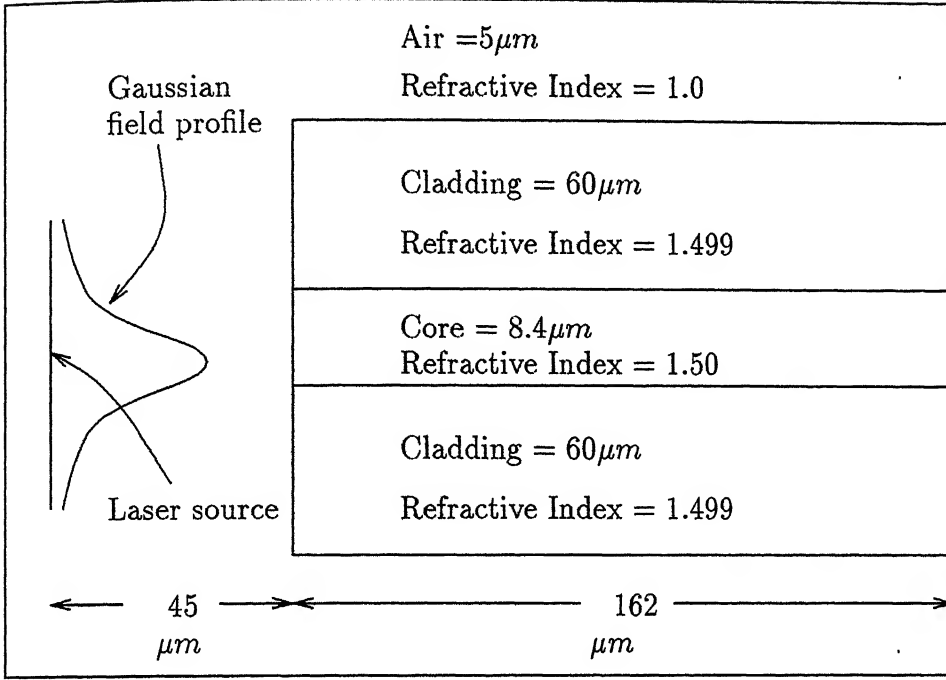
Figure 3.5: A simple coupling model. Spot size of the Gaussian beam = μm.

3.2.1 Software Implementation

The main structure of the programming outline for model–1 is similar to that for studying the point source. In this case the dielectric constants for the nodes of the whole computation domain should be defined carefully. Some special treatments should be taken for the nodes at the boundaries between two media. It can be proved that for the fields at the nodes on an interface between two media, the effective dielectric constant becomes $\frac{\epsilon_1 + \epsilon_2}{2}$, for three media, it becomes $\frac{\epsilon_1 + \epsilon_2 + \epsilon_3}{3}$ and so on; where ϵ_1, ϵ_2, ϵ_3 etc. are the dielectric constants of the different media. A proof of the above statement is given in Appendix A for an interface seperated by two media only. That is why, for the boundaries between the core-cladding, core-air and air-cladding, an average value of the permittivities is used. The source condition is the same as given by the eqn. (3.1). To apply the boundary conditions different phase velocity should be considered for different media. However, the programming outline for model–1 can be given by the following steps.

1. Begin:

   • INPUT PARAMETERS:

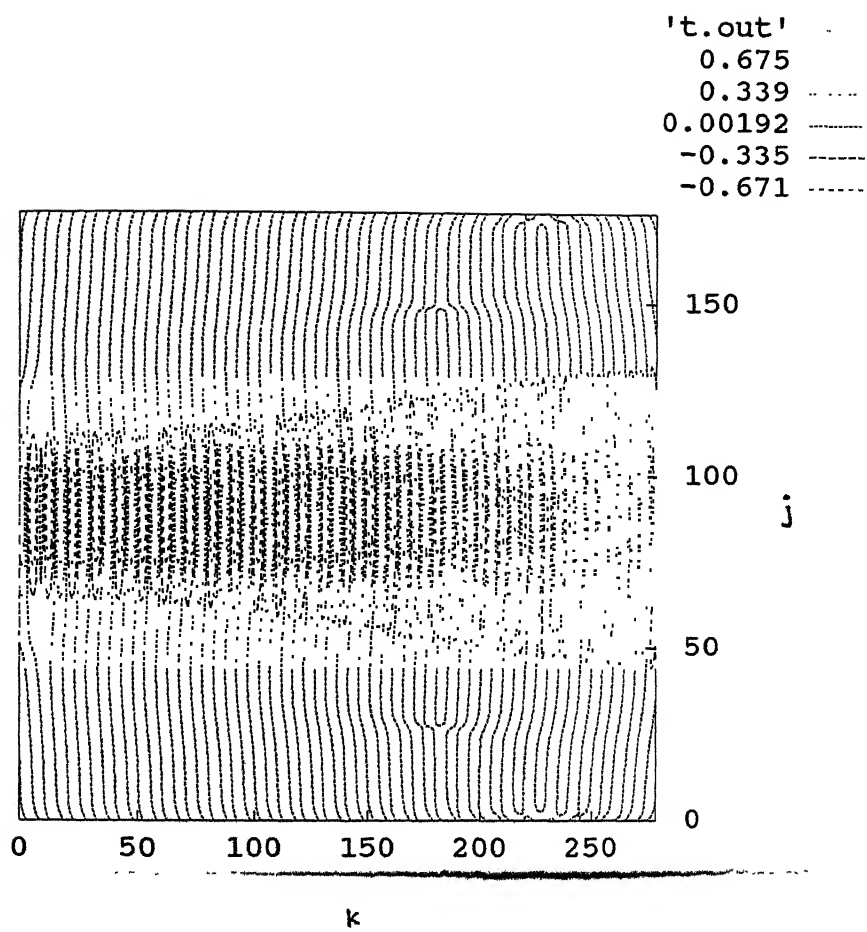Figure 3.6: Contour plot of the electric field between source and fiber-end for model −1.

2. Read: number of nodes in air on both sides of the waveguiec in y–direction (y_{0max}), number of nodes in cladding on both sides of the core (y_{1max}), number of nodes in the core region in the y–direction (y_{2max}), number of nodes between the source and the coupling end of the waveguide in z–direction (z_{1max}), no. of nodes in fiber in z–direction (z_{2max}), operating wavelength (λ) of the source, dielectric constant of the air (ϵ_0), dielectric constant of the core (ϵ_1), dielectric constant of the cladding (ϵ_2) and permeability of the media (μ_0).

   • SELECTION OF SOME PARAMETERS FOR THE FD–TD METHOD:

3. Calculate: phase velocity in the air(v_{p0}) = $\frac{1}{\sqrt{\mu_0 \epsilon_0}}$, phase velocity in the core (v_{p1}) = $\frac{1}{\sqrt{\mu_0 \epsilon_1}}$ and phase velocity of the cladding (v_{p2}) = $\frac{1}{\sqrt{\mu_0 \epsilon_2}}$

4. Select: maximum phase velocity (v_{pmax}) = v_{p0} = $max < v_{p1}, v_{p2}, v_{p0} >$

5. Select: $\delta y = \delta z = \delta = \frac{\lambda}{10}$ and $\delta t = \frac{\delta}{2\,v_{pmax}}$

6. Select different dielectric constants for the different nodes depending on the region in which the nodes are located.

7. Take an average value of the dielectric constants for the nodes at the interfaces between different media.

8. Select: no. of time steps (n_{max})=maximum of the no. of time steps required to reach the wave at the boundary in the y–direction from source and no. of time steps required to reach the wave at the boundary in the z–direction from the source.

   • STARTING OF THE CALCULATION OF THE FIELD COMPONENTS:

9. Start time stepping (n) at $n = 0$

10. Choose a line along y–axis (j, k_0) (say). Apply input along this line as given by the equation 3.1. Source should be located as far away from the boundary as possible.

    • CALCULATION OF THE FIELD COMPONENTS AT THE INTERIOR NODES:

11. Calculate $H_y(j,k)$, $H_z(j,k)$ and $E_x(j,k)$ at the interior nodes of the computation domain with the regular finite difference scheme.

    • SPECIAL TREATMENTS FOR THE BOUNDARY NODES:

12. Apply Mur's second order ABC to calculate the electric field components at the boundary nodes. Different phase velocities are considered at different nodes on the boundaries for different media.

13. Increase n by one i.e. $n \rightarrow n + 1$

14. Verify: if $n \leq n_{max}$ then go to step (9); else finish.
    • CALCULATION OF THE FIELD ENVELOPE:

15. Compute the time period (T) of the sinusoidal input. Calculate the no. of time steps (n_{env}) in half cycle (T/2).

16. Find the maximum of the field components at each node during the final n_{env} time steps. This will give the envelopes of the corresponding field components.

17. Print output.

18. End

3.2.2 Results

First, we present the result for the field characteristics between the source and the coupling end of the waveguide. In Figure 3.6 we present the contour plot of the electric field within the region between the source and the fiber-end considering the model given in Figure 3.5. The contour plot for the electric field is already given when there is no fiber i.e. propagation of Gaussian beam in free space, in Figure 3.4 for the same computation domain as between the source and fiber-end. If we compare the two contour plots we can see the differences easily. From Figure 3.4 we see that the phase fronts are very regular when the Gaussian beam propagates in free space. But from the Figure 3.6 we see that phase phase fronts are not regular and a weak interference pattern is generated. This is mainly due to the reflection ocurred at the air-core and air-cladding interfaces.

In Figure 3.8 we present the electric field profiles taken at three positions within the source-fiber region. From these profile plots we see that the difference between the field profile at $Z = 7.5 \mu m$ and $Z = 18 \mu m$ is very less but there is a significant difference between the above two and the plot at $Z = 30 \mu m$. These are the envelope plots which show the variation in amplitudes only.
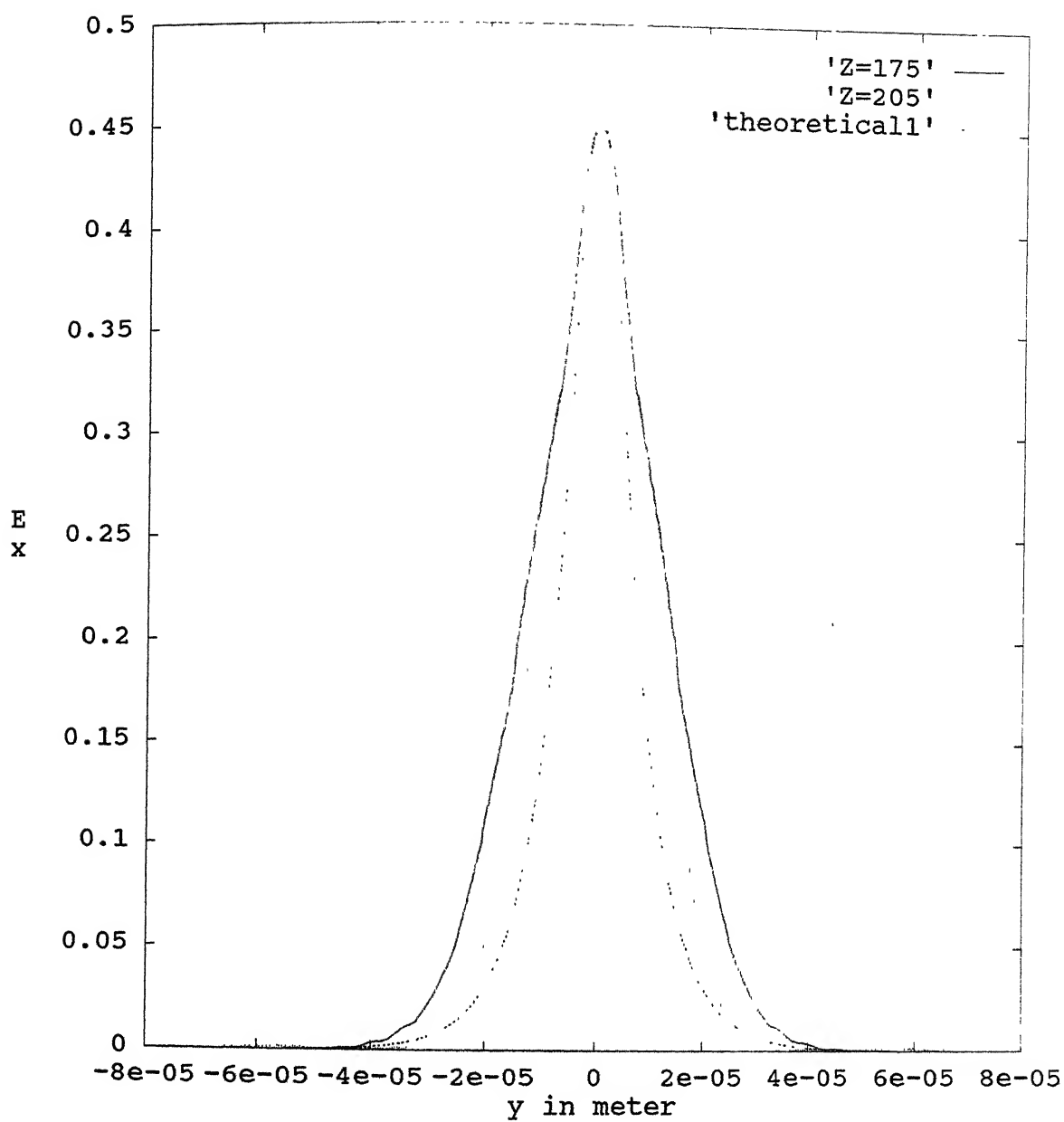
Figure 3.7: Fundamental field profiles for model–1. Z=175 for $175\mu m$ and Z=205 for $205\mu m$ from the source.
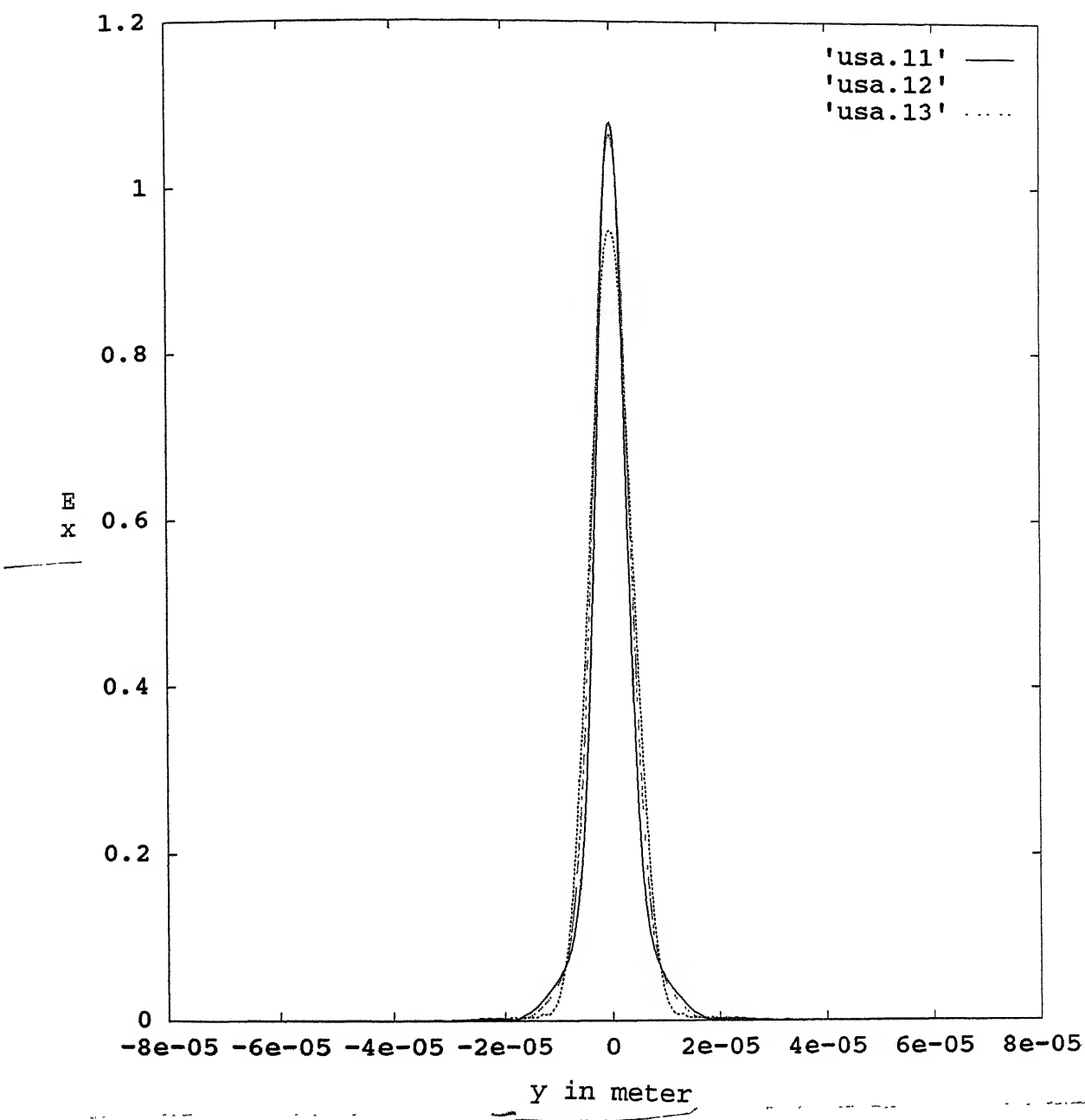
Figure 3.8: Field profiles within the source-fiber region for model–1. usa.11 for $Z = 7.5 \mu m$; usa.12 for $Z = 18 \mu m$; and usa.13 for $Z = 30 \mu m$ from the source, respectively.
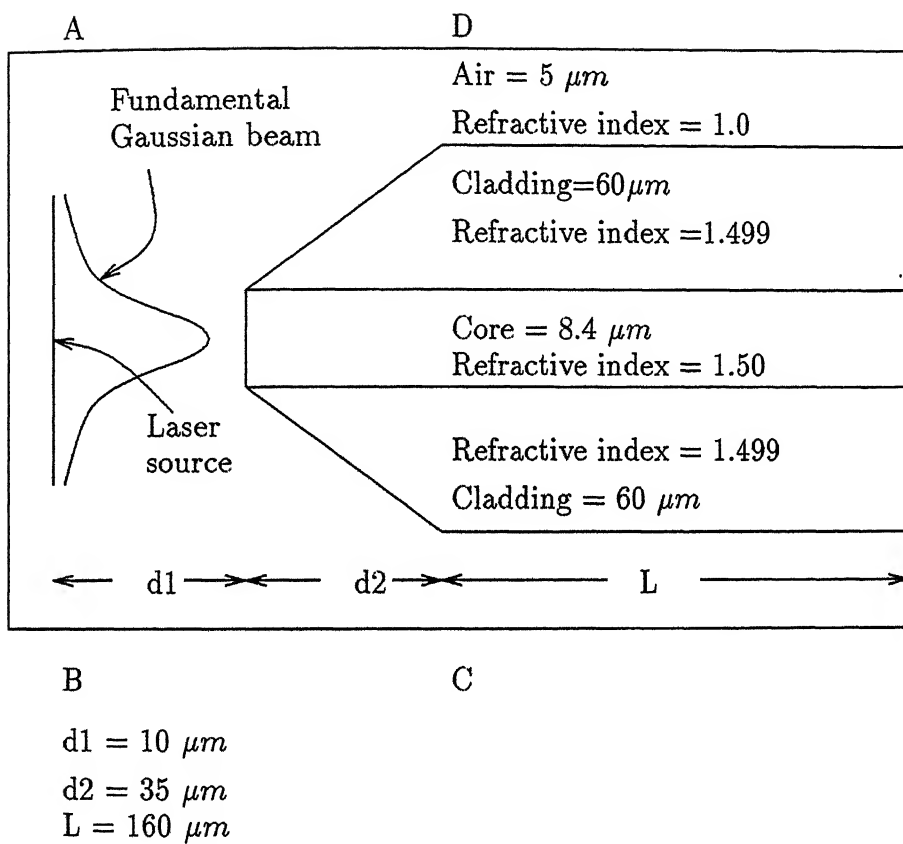
Now we present the fundamental field profile within the waveguide and the coupling efficiency. A theoretical treatment of the fundamental mode profile for TE mode in a symmetric planar waveguide is given in appendix B. In Figure 3.7 we present the fundamental field profiles within the waveguide at the distances $Z = 175\mu$ and $205\mu m$ from the source along with the theoretical value. From the figure we see that the field profile within the core is similar to that of the theoretical one. But within cladding region the field profile deviates to some large extent from the theoretical value. This is mainly due to the short length of waveguide under consideration. Over which the evanescent fields in the cladding region have not settled down to the final equilibrium values. Usually it takes about $50m$ distance for the evanescent fields to the equilibrium value resulting resulting in propagating modes. It is practically impossible to simulate over $50m$ long by the FD-TD method. For the field profile obtained at $Z = 205\mu m$ is used to calculate the coupling efficiency of this model. The coupling efficiency obtained by this model is only 38.5027%. The maximum obtainable theoretical coupling efficiency is 65.23% (see Appendix C). This dissimilarity is mainly due the planar structure consideration of the fiber. Moreover, we have considered a very short length of the fiber which is practically impossible to set up a particular mode within the fiber. Further, for the theoretical consideration cladding is assumed to be extended to infinity whereas a finite value is considered for our study. A small error is also introduced by the FD-TD method.

3.3   Study Of model-2

In this section we study a different type of coupling model in which taper-ended fiber is used to couple power from the source. One of the models of this type is shown in Figure 3.9. The dimensions and the refractive indices are mentioned in the figure.

3.3.1   Software Outline: An Extra Treatment

The main programming outline for model-2 is exactly the same as for model-1 except the tapper portion of the fiber. The extra care is taken only to define the dielectric constants for different nodes within different regions carefully. In this case the extra tapper portion is discretized using stair case approximation. The input parameters and other things are same as for model-1. That is why in this section we present only the discreatization procedure of the tapper portion of the fiber. The tapper portion is shown in Figure 3.10. To define

A

D

Fundamental
Gaussian beam

Air = 5 μm

Refractive index = 1.0

Cladding=60μm

Refractive index =1.499

Core = 8.4 μm
Refractive index = 1.50

Laser
source

Refractive index = 1.499

Cladding = 60 μm

← d1 →← d2 →← L →

B

C

d1 = 10 μm

d2 = 35 μm

L = 160 μm

(Drawn in arbitrary scale)

Figure 3.9: Model–2: coupling with taper-ended fiber. Spot size of the Gaussian beam =μm.
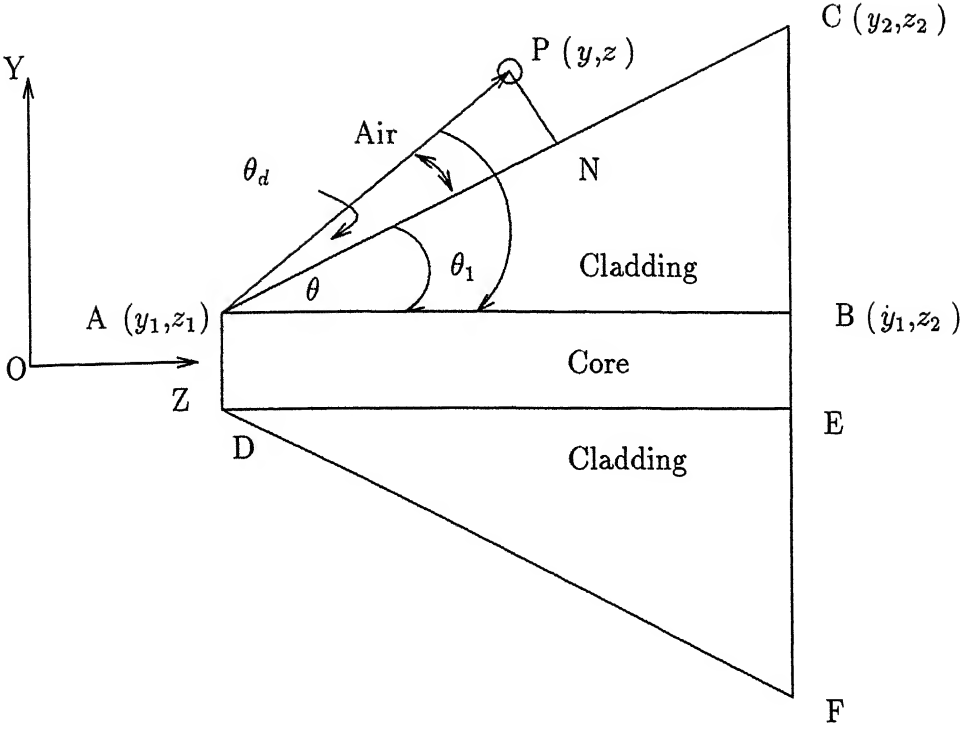
Figure 3.10: Tapper portion of the fiber of model–1.

dielectric constants for the region ADEB is very easy. But, for the regions ABC and DEF, we use the following method. Suppose P (y,z) is a point located anywhere in the left-side region of CF. The slope of the line AP is given as

$$m = \tan(\theta) = \frac{z - z_1}{y - y_1}$$

Now the slope of the line AC is fixed for a perticular structure. This slope is given as

$$m_f = \tan(\theta_1) = \frac{z_2 - z_1}{y_2 - y_1}$$

If $m > m_f$, the point P is located within the air; otherwise it is located within the triangle ABC(cladding). The nodes at the interfaces are selected in the following. From the point P draw the perpendicular PN on the line AC. Let the angle between the lines AC and AP be θ_d. Now, if a point satisfies the constraint

$$PN = AP \ \sin(\theta_d) \leq \frac{\delta}{2}$$

we consider this point as the interface point between the air and the core for the stair case approximation of the interface; and we assign an average dielectric contant for this point.

Using the above idea we can select the nodes within the core, cladding and air. The same rule is also applied for the region DEF. After selecting the nodes for different regions we can assign different dielectric constants for different nodes. For the nodes at the interface between different media we use an average dielectric constants as mentioned earlier.

3.3.2 Results

Now we present the results for model–2. In Figure 3.11 we present the contour plot of the electric field within the region ABCD as shown in the figure. From the contour plot we see that a strong reflection occur at the air-core and air-cladding boundaries. As the angle of
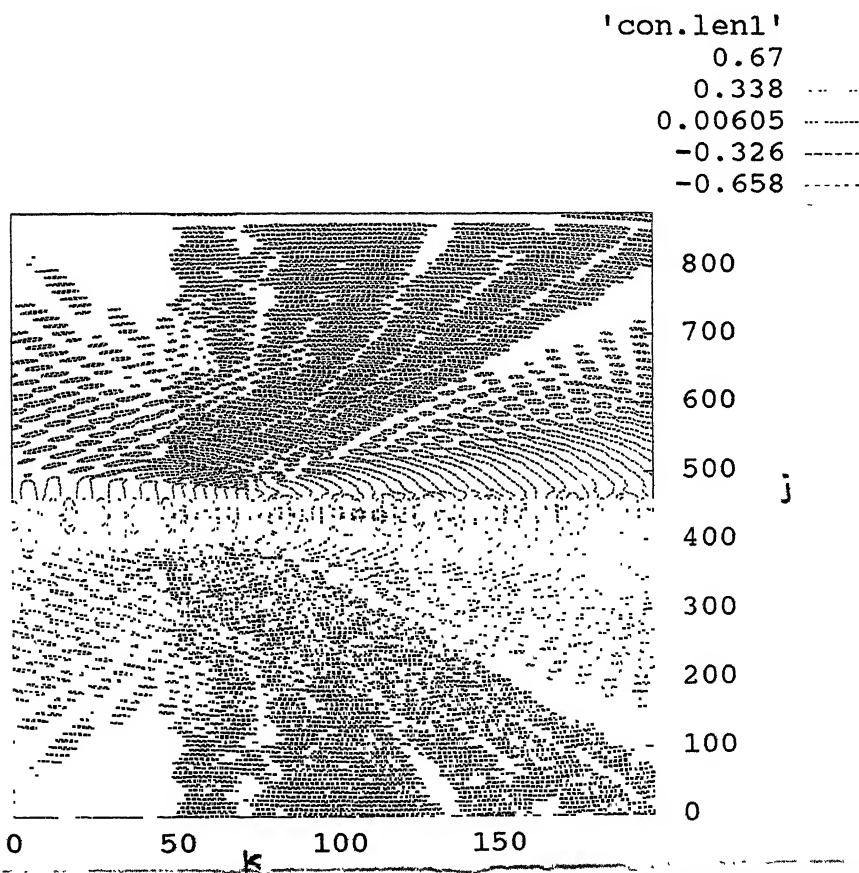
Figure 3.11: Contour plot within the source-fiber region of the electric field for model–2

incidence of wave is different for the different points of the taper portion of the fiber, different amount of energy is reflected from different sections. Most of the energy is reflected from the taper portion of the fiber. Due to the normal incidence of the field on the core region, a small portion(maximum 4%) of the energy is reflected. Therefore, a narrow field is propagated

Figure 3.12: Fundamental field profile plots at $Z = 205\mu m$ from the source for model–2

through the core of the fiber. Source condition and air-core, air-cladding and core-cladding boundaries are treated in the same way as before. In Figure 3.12 the fundamental field profile for $Z = 205\mu m$ from the source is plotted along with the theoretical plot. If we compare Figure 3.7 and Figure 3.12 we see that field profile for model-2 is more accurate both in core and cladding to the theoretical value than model-1. The 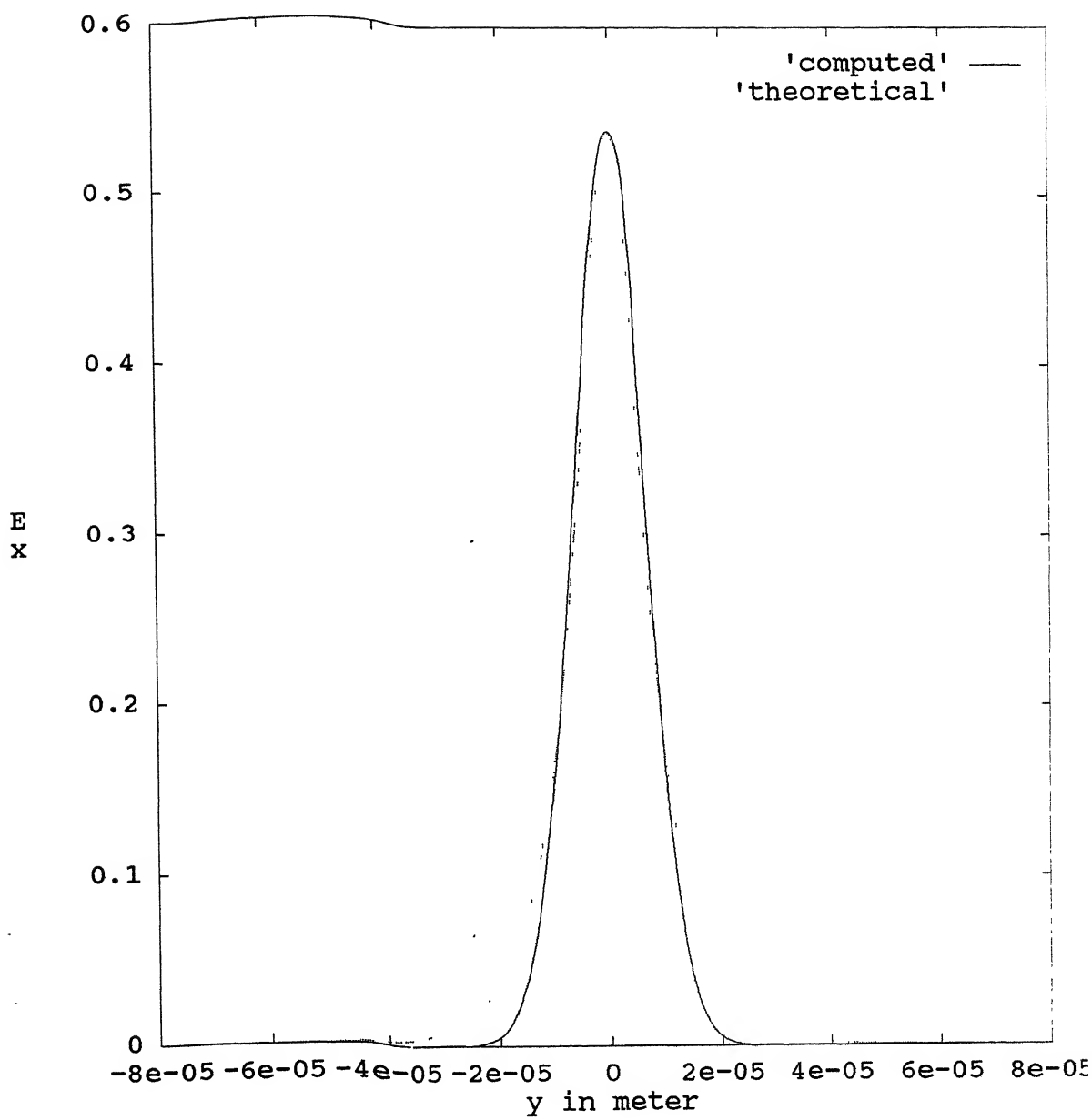coupling efficiency obtained by this model is 51.937%. In this case we see that there is an improvement of the coupling efficiency over the butt coupling. This is due to the fact that a narrow field is entered into the fiber and the taper portion acts somehow as a lens. In practical cases coupling from semiconductor laser into single mode fibers is done with tapered hemispherical ends[21]. The taper-end of the fiber collects most of the energy in the core region and that is why a strong field is propagated through the core and increase the coupling efficiency.
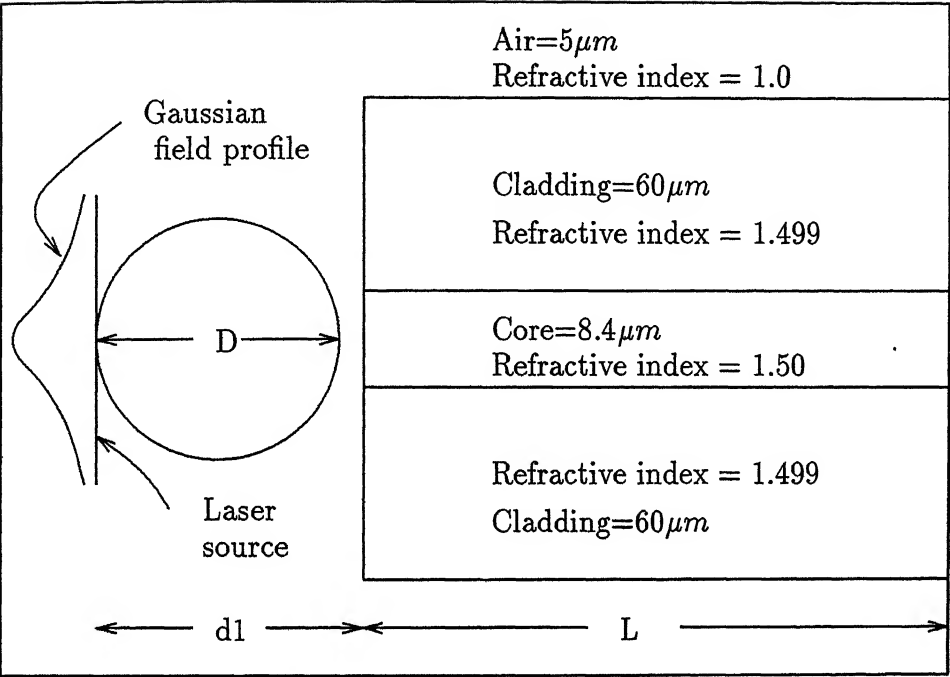
3.4   Study Of Model-3

In this section we study a good model using a nonimaging microsphere[23,24] between the optical source and fiber as shown in Figure 3.13. First we make some assumptions: the sphere lens has refractive index $n_l = 2.0$ and outside medium is air (refractive index $n_{om} = 1.0$). Then the focal length can be calculated from the gaussian lens formula [30]

$$\frac{n_l}{s} + \frac{n_{om}}{q} = \frac{n_{om} - n_l}{r} \tag{3.6}$$

where s and q are the source and image distances, respectively, as measured from the lens surface, and r is the radius of curvature of the lens surface. The following sign conventions are used to solve the eq. (3.6):
• Light travels from left to right.
• Object distances are measured as positive to the of a vertex and negative to the right.
• Image distances are measured as positive to the right of a vertex and negative to the left.
• All convex surfaces encountered by the light have a positive radius of curvature, and concave surfaces have anegative radius.

Using these conventions we now find the focal point for the right-hand surface of the lens shown in the Figure 3.13. To find the focal point, we set $q = \infty$ (for collimated output) and solve for s in eqn. 3.6, where s is measured from point B. With $r = -D/2$, eqn. 3.6 yeilds

Air=$5\mu m$
Refractive index = 1.0

Cladding=$60\mu m$
Refractive index = 1.499

Core=$8.4\mu m$
Refractive index = 1.50

Refractive index = 1.499
Cladding=$60\mu m$

d1=$45\mu m$
L=$160\mu m$

(Drawn in arbitrary scale)

Figure 3.13: Nonimaging microsphere is placed between the source and the fiber; model–3

$s = f = D$. Thus the focal point is located on the lens surface at point A. This, of cource, changes if the refractive index of the sphere is not equal to 2.0.

That is why for $n_l = 2.0$ the source should be placed close to the surface of the lens and fiber can be placed right side of the lens surface. Generally the fiber is also placed as close to the lens as possible for the compact packaging purpose.

The use of homogeneous glass microsphere lenses has been tested in a series of several hundred laser diode assemblies by Khoe and Kuyt [26]. Spherical glass lenses with a refractive index of 1.9 and diameters ranging between 50 and $60\mu m$ were epoxied to the ends of $50\mu m$ core-diameter graded-index fibers. Coupling efficiencies in these experiments ranged between 50 and 80 percent.

3.4.1 Software Outline: An Extra Treatment

In this case also the main programming structure is the same as model–1 except the lens between the source and waveguide. Extra treatment is required only to define the dielectric constants for the nodes in the lens material instead of the air between the source and the waveguide. In two dimensional configuration the lens is assumed to be a cylindrical with a circular cross section on the y–z plane. Therefore we discuss the extra treatments required for the lens. To select a node inside or outside of the lens material (i.e. in air region) we use the rule as follows. The equation of a circle in y–z plane can be given as

$$y^2 + z^2 = r^2$$

where r is the radius of the circle. Let P(y,z) be any point within the region between the source and the waveguide. Now, if

$$y^2 + z^2 - r^2 < 0$$

then the point is located within the circular region; otherwise it in the outside of it (i.e. in air). For points at the interface between the lens material and the air we use the following condition

$$|y^2 + z^2 - r^2| \leq \frac{\delta}{2}$$

Now we can select the location of the different nodes and assign different dielectric constants depending on the medium in which it is located. For the interface nodes an averaging rule of the dielectric constants is used.

3.4.2 Results

We have studied the lens with refractive index $n_l = 2.0$, diameter $D = 42\mu m$;and for a step index fiber by the FD–TD method. Fiber is placed just $1.5\mu m$ right of the point A. The input condition is the same as given by 3.1. In Figure 3.14 we present the contour
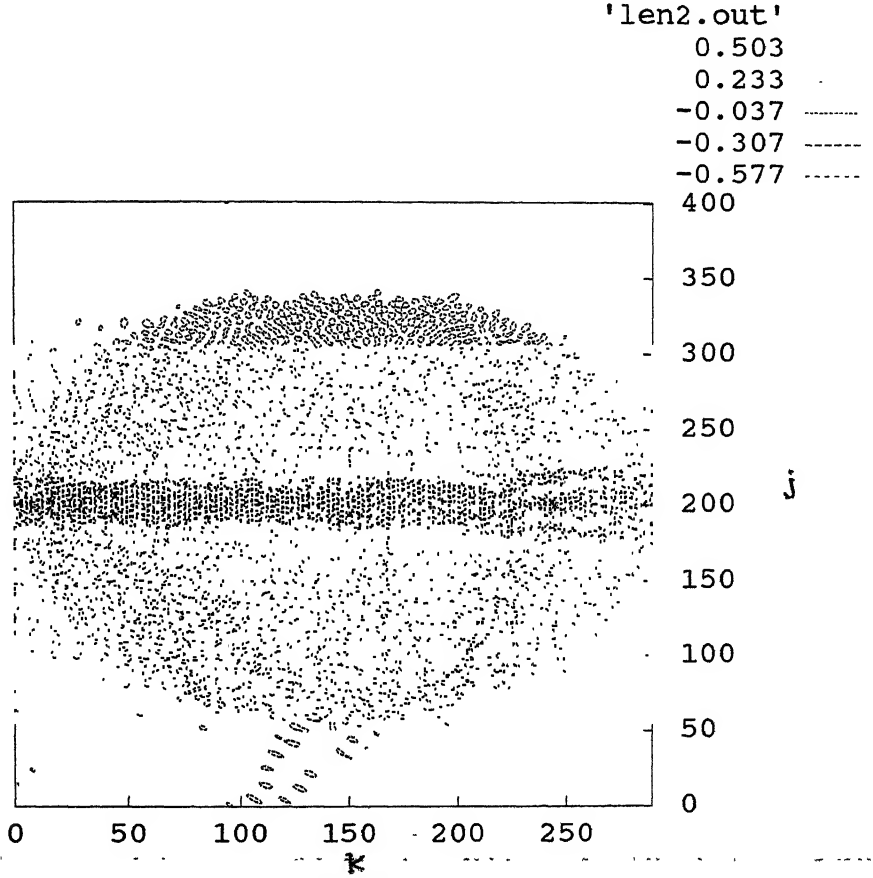

Figure 3.14: Contour plot of the electric field for model–3

plot of the electric field to see the field pattern generated between the source and the fiber. From Figure 3.14 we see that as the field propagates towards the fiber coupling end a part of the input energy is reflected at the lens-air interface. A part of the energy is also reflected from the air-core and air-cladding interfaces. Maximum 30% of the input field amplitude is reflected for normal incidence but different amount of energy is reflected from different points of the lens surface due to different angle of incidence at different points. The most important thing is to note that inspite of the reflection occured at the interface of the air and the lens material, a strong field is propagated through the lens material towards the fiber along the z axis and this actually shows the improvement of the coupling efficiency of this lensing scheme.

The fundamental field profile is presented in Figure 3.15. From this figure we see that again
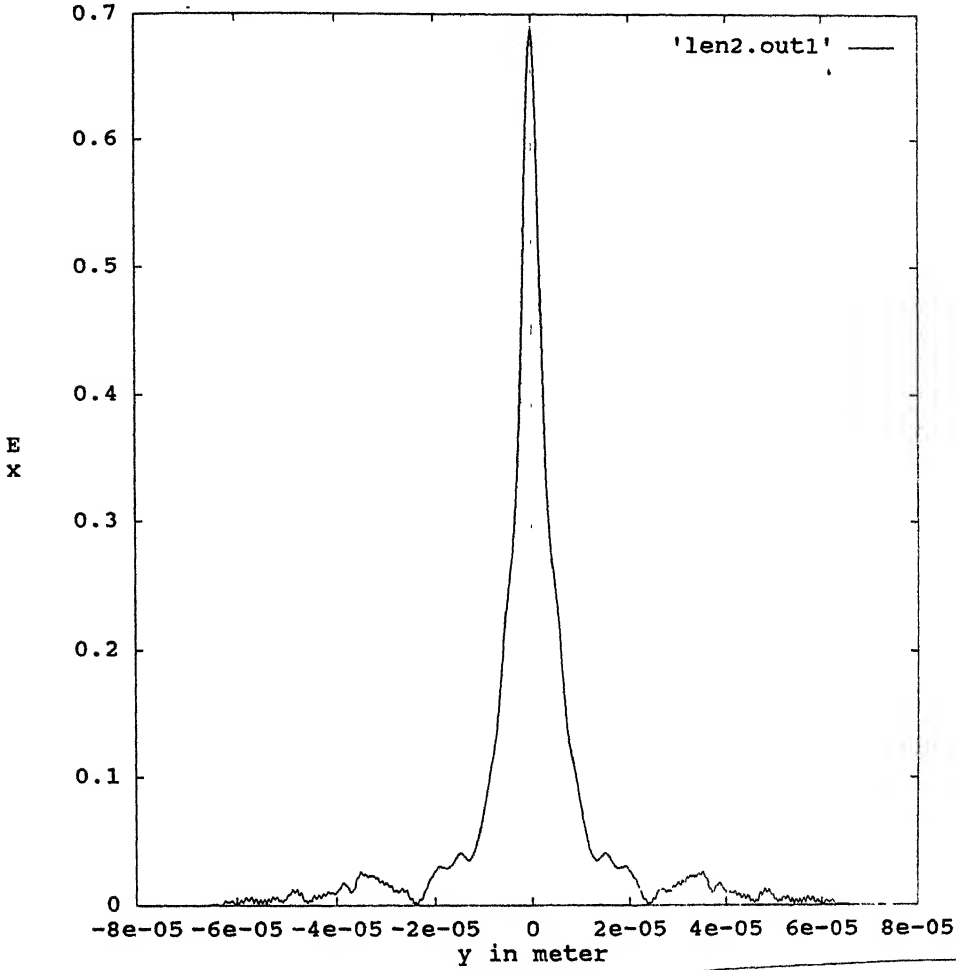

Figure 3.15: Fundamental field profile at $Z = 205\mu m$ from the source for model–3.

the field is not stable in the cladding region but the field within the core is almost stable. We also observe from Figure 3.15 that in this case most of the energy is confined within the core region. For this model the efficiency obtained by the FD–TD method is 69.394%. In this case we see that the coupling efficiency is the highest among all the three coupling attachments. This is mainly due to the the magnification of the emitting surface area of the source by the lens [29, chapter-5]. The field profiles in between the lens and the fiber is shown in the Figure 3.16. We see from the figure that a narrow field enters into the fiber. If there is no lens, due to the diffraction effect the width of the light beam spreads out resulting in a small amount of energy incident on the core of the fiber. But, owing to the presence of the lens light beam does not spread out and therefore a strong field is propagated through the fiber.
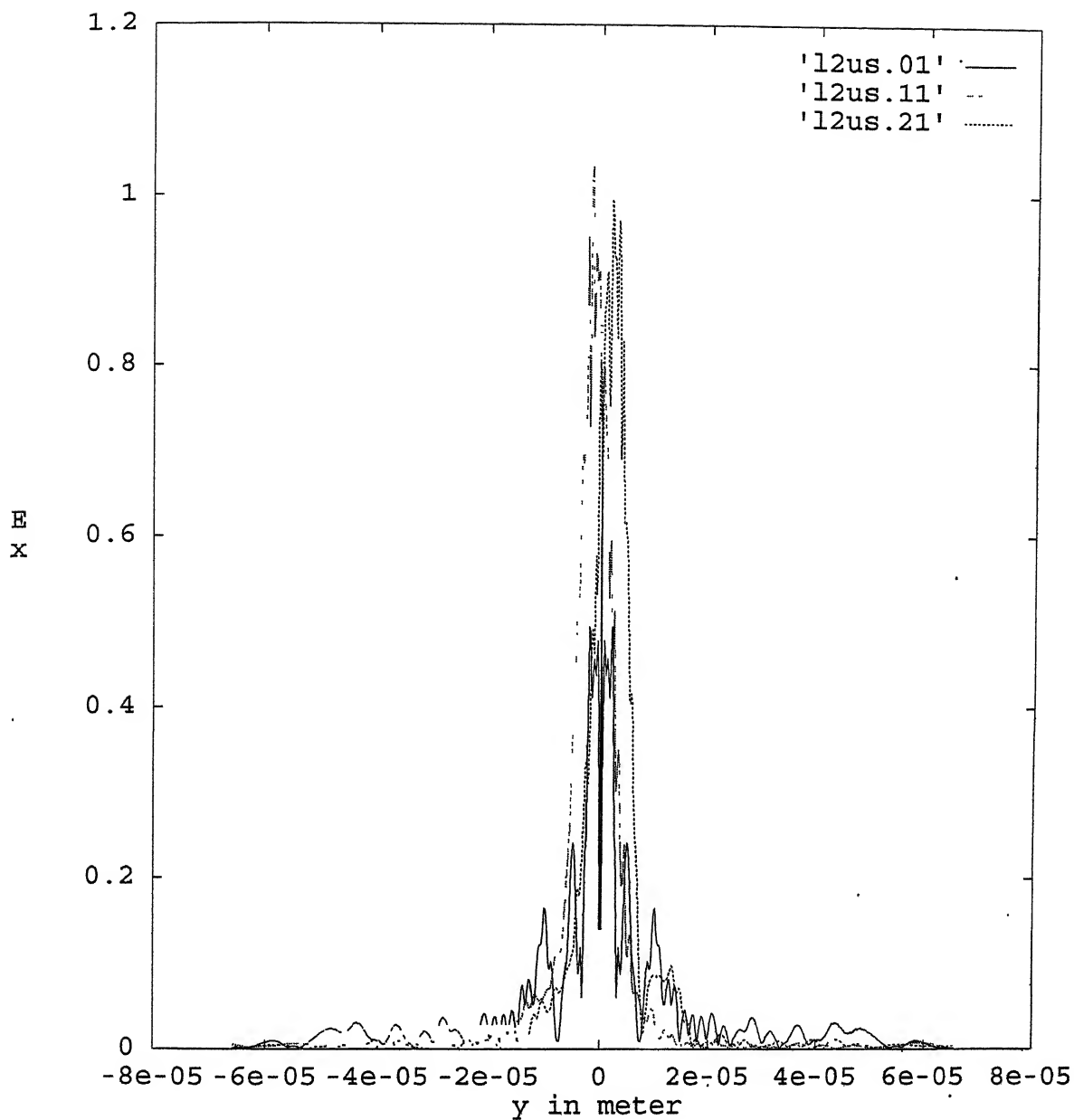
Figure 3.16: Field profiles in between the lens and fiber for model–3. l2us.o1: for no shifting; l2us.11 for shifting the source 3.0 μm in the downward direction; and l2us.21 for shifting the source 1.5 μm in the upward direction.

That is why in this case the coupling efficiency is much higher than the other two cases.
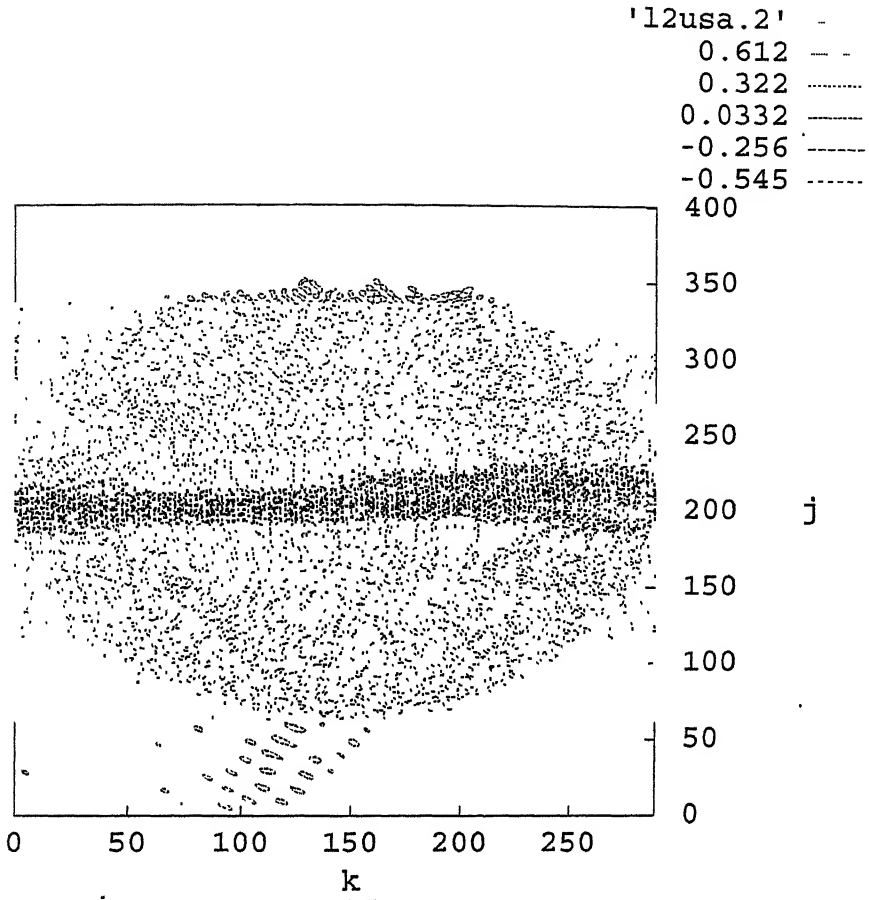

Figure 3.17: Contour plot of the electric field for 1.5μm shifting of the source in the downward direction laterally.

Now we present the results for the misalignment problems. From the field profiles in between the lens and the fiber end face presented in Figure 3.16 for the shifting of the source in the downward and upward directions, we see that due to the shifting field strength is increased before the cladding regions. Moreover, the light beam spreads out due to the shifting. That is why, less energy is propagated through the core of the fiber. The contour plot of the electric field within the source-fiber region is presented in Figure 3.17 when the source is shifted 1.5μm in the downward direction laterally. If we compare Figure 3.14 with Figure 3.17 we can easily see that less amount of energy is propagated through the lens towards the fiber. In Figure 3.18 we present three field profiles at $Z = 205\mu m$ from the source: 12us.o3 for no shifting, 12us.13 for the source shifted 3μm in the downward direction and 12us.13 for the source shifted 1.5μm in the upward direction. Due to the shifting of
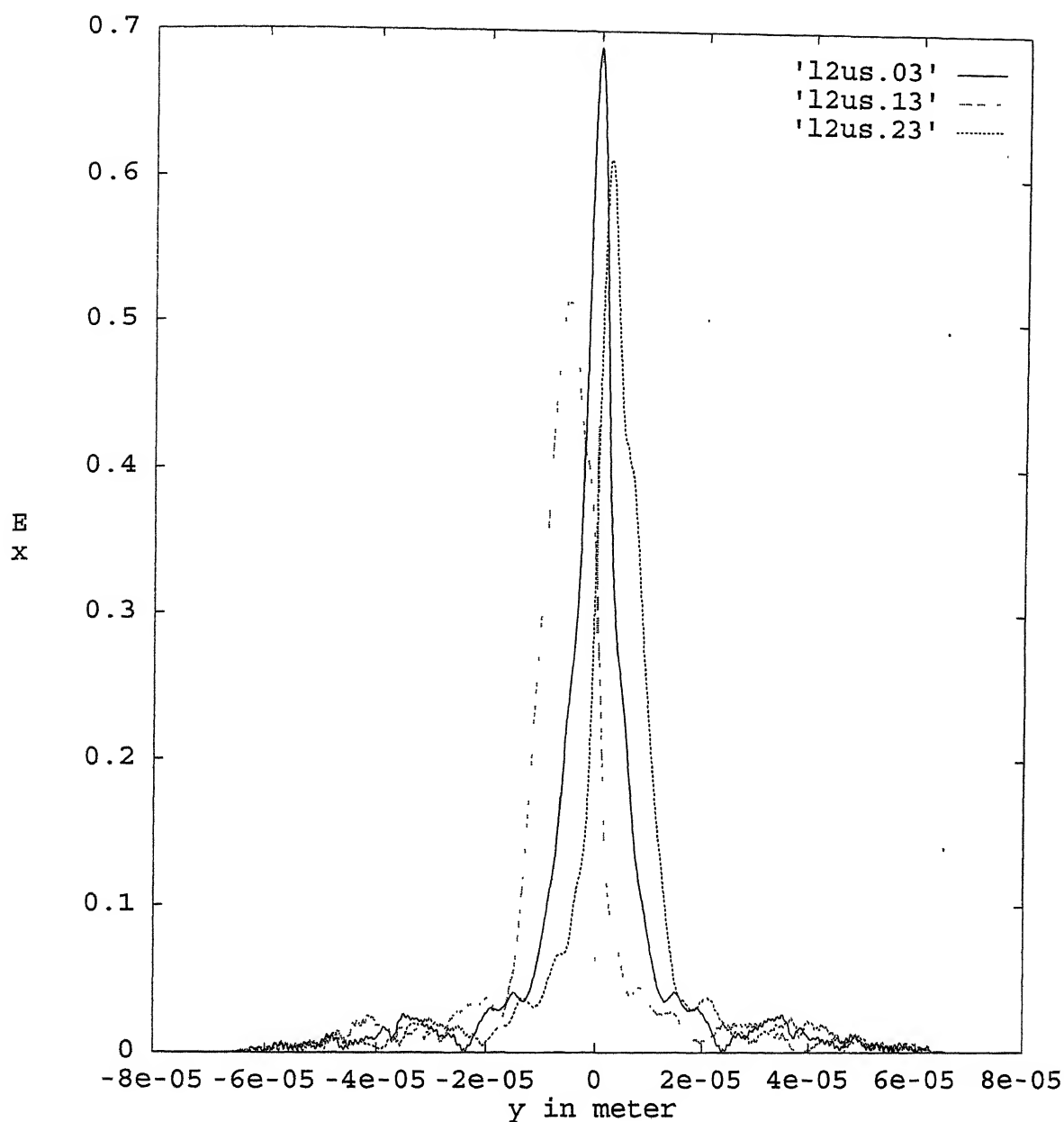
Figure 3.18: Field profile plots for the misalignment problem for model–3. l2us.03: for no shifting of the source; l2us.13: for shifting the source 3.0 μm in downward direction; and l2us.23: for shifting the source 1.5 μm in the upward direction.

the source, we see that the amplitude of the field is reduced significantly. For l2us13 and l2usa13 the coupling efficiencies are 33.436% and 54.193%, respectively, while for no shifting this is 69.394%. Therefore, the coupling efficiency is reduced for the shifting of the source significantly. Further the power propagated through the cladding region is increased in this case and cladding fields are not in equilibrium state due to the short length of the fiber under consideration.

3.5   Conclusions

In this chapter we have given the field characteristics between the source and the planar optical waveguide for three coupling attachments. We have also studied the coupling efficiencies for different coupling models. We see that for model–1, the coupling efficiency is 38.5027% which is large enough compared to the practical coupling results for actual fibers. For actual fibers the coupling efficiency lies between 10 and 20 %. For model–2 we get the coupling efficiency 51.937% which supports the practical results. Practically, the power coupling from a semiconductor laser into single mode fibers with hemispherical ends gives the coupling efficiency between 40% and 70%. We see from model–3 that coupling efficiency is the highest among all the three coupling attachments under our considerations. In this case we get the coupling efficiency is 69.394%. For the actual fiber this efficiency lies between 50% and 70%.

The first configuration is the simplest one. It is very easy to handle for practical experiments. The second coupling arrangement is sensitive to the proper mechanical alignment and creat additional complexities for the practical cases. The third coupling arrangement creats more complexities than the other two. One problem is that the lens size is similar to the source and fiber core dimensions, which introduces fabrication and handling difficulties. But, for the efficient coupling the last coupling arrangement is the best among the three as it gives the highest coupling efficiency.

We have also developed the visualisation soft-ware package to see the optical field characteristics within the source-fiber region of the transmitter packages. The advantages of this package are: (1) we can change the parameters i.e. the refractive indices of the core, cladding and the medium within the source-fiber region, length of the fiber, wavelength of the source, distance between the source and fiber, dimensions of the core and cladding regions, source

emitting area etc. can be changed as these are given as the inputs to the programming; (2) The absorbing boundary condition is very simple and easy to implement. (3) Soft-ware is written in FORTRAN 77 which is also easy to handle and understand. Using this soft-ware we can study the reflection characteristics of the field from the fiber end and the coupling efficiency for different transmitter packages. Varying the input parameters it is possible to find out a particular arrangement condition for a particular transmitter package for which an efficient coupling can be achieved. Following this optimum coupling condition, one can design this particular transmitter package for the practical purpose so that maximum coupling of power can be obtained. Moreover, this soft-ware can be used to study the effect of the mechanical misalignment for the fiber optic transmitter packages.

Chapter 4

Further Scope Of Work

In this chapter we present the further scope of work for which our results and discussions may be used as the initial required background. Using the FD–TD method and Mur's ABC, we have studied the optical field characteristics within the region between the source and the fiber for only three coupling configurations. Following the same approach, we can study the field charateristics and the coupling efficiencies for other coupling configurations as suggested in the first chapter. Moreover, the results can also be extended for three dimensional configurations. But, in this case the major difficulties are the requirement of a large amount of computer memory and computation time. One may study the coupling problem for the three main types of lenses discussed in the following section.

4.1 Three Main Lenses For Coupling

Now we present three main types of single-element lenses for fiber-optic devices; (1) quarter-pitch GRIN-rod lens; (2) ball lens and (3) rod lens. These three lenses are very useful fiber-optic devices which can be used for the optical power coupling from the source into the fiber and from fiber to fiber.

4.1.1 GRIN-Rod Lens:

The refractive index in a GRIN-rod lens is given by

$$n^2(r) = n_0^2[1 - (g\,r)^2 + h_4\,(g\,r)^4 + h_6\,(g\,r)^6],$$

where $n(r)$ =refractive index at distance r from the axis;

n_0 =refractive index on the axis;
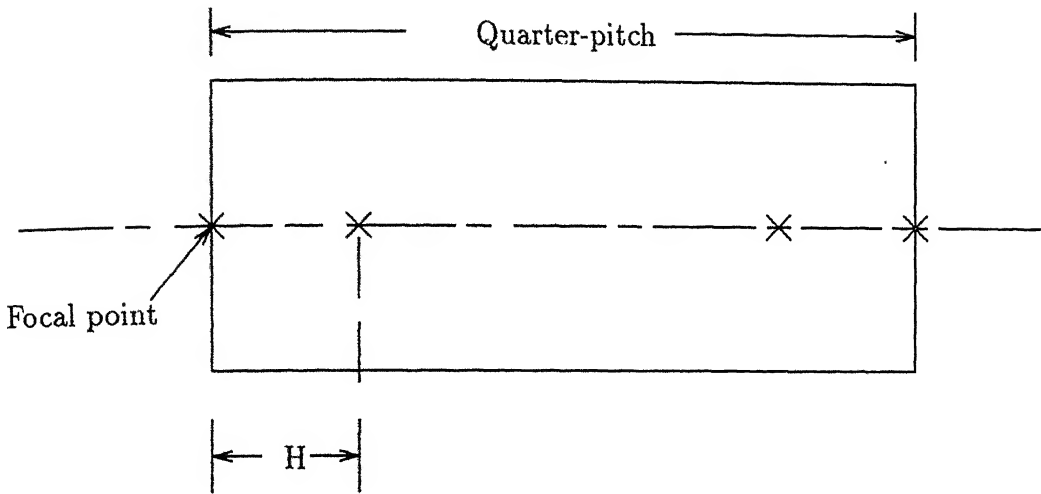
Figure 4.1: Fundamental imaging parameters of the GRIN-rod lens.

g =focusing constant; and

h_4, h_6 =higher order constants.

For paraxial rays the higher order terms with coefficients can be neglected. A ray incident on a GRIN-index lens travels along sinusoidal curve with a periodic length (pitch)= $\frac{2\pi}{g}$. For the usual quarter-pitch lens, the focal length and the position of the principal points H are (Figure 4.1)

$$f = \frac{1}{n_0\, g}$$

$$H = \frac{1}{n_0\, g}.$$

4.1.2 Ball Lens:

A ball lens is fully described by its refractive index and radius r. Application of the thick lens formula leads to (Figure 4.2)

$$f = \frac{n}{2(n-1)} r,$$

$$H = r.$$

4.1.3 Rod Lens:

One focal point of the rod lens is chosen at the plane face of the lens, so that only independent parameters are refractive index n and radius of curvature r (Figure 4.3). Using the thick lens

51

Figure 4.2: Fundamental parameters of the ball lens.
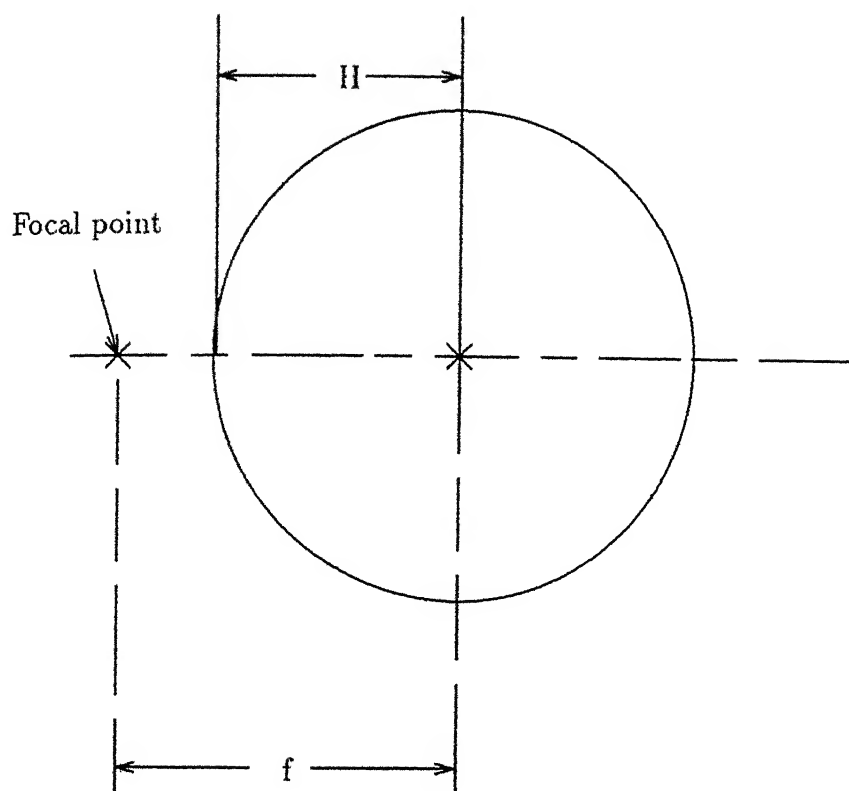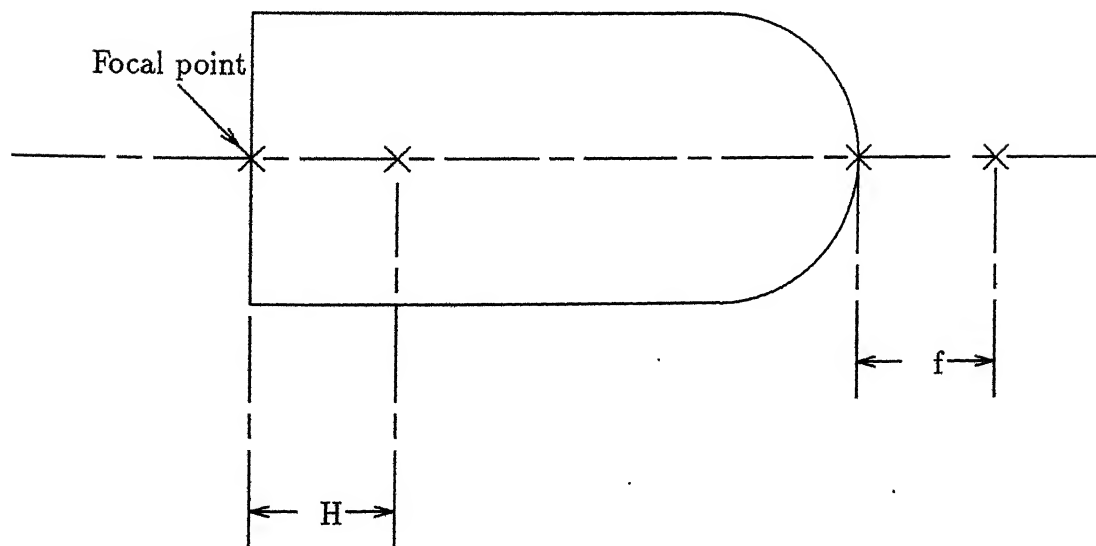

Figure 4.3: Fundamental parameters of the rod lens.

formula we get,

$$f = \frac{1}{n-1}r,$$

$$H = \frac{1}{n-1}r$$

4.1.4 Complete Lens System:
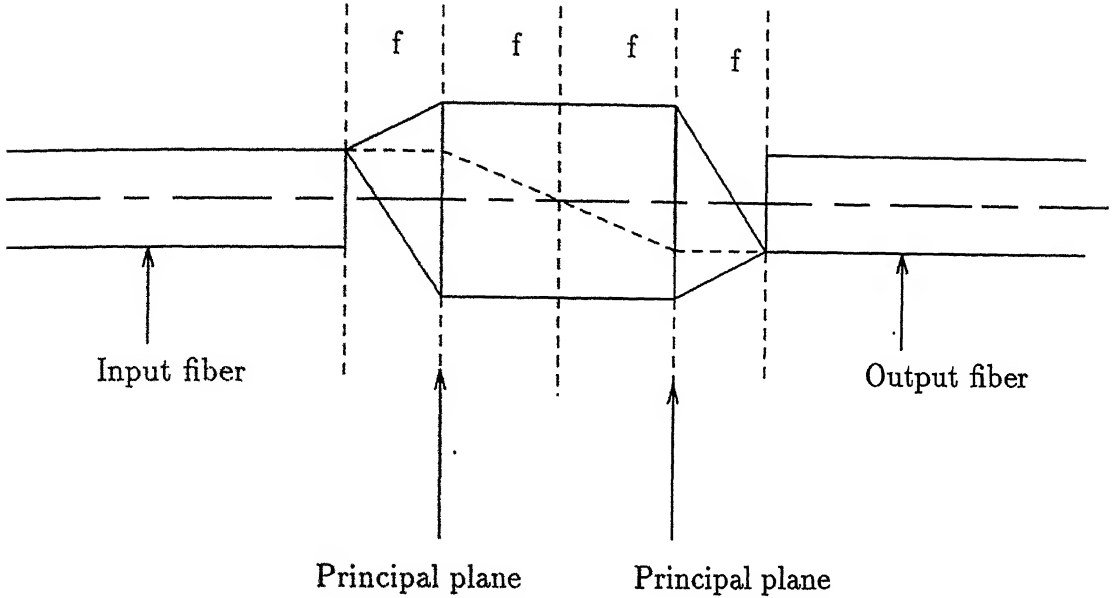
Figure 4.4: Universal arrangement for optimal lens coupling.

For a maximum coupling between the source and the fiber or between the fibers, an one to one image should be made of the emitting surface upon the receiving one. For fiber to fiber coupling, special consideration should be taken so that the launching angle with the fiber end face has to be the same at the receiving fiber end. All these conditions are satisfied only if the ends are positioned in the focal plane while the foci of the lenses coincide (Figure 4.4). The incoming light cone is tilted if the foci of the lenses do not coincide. In a proper design, this tilt angle should always be small compared with the numerical aperture of the fiber.

In a well designed lens coupling each currently proposed lens type i.e. GRIN-rod lens, ball lens, and rod lens, will reach equal imaging quality and hence equal couple efficiency. For typical communication fibers, coupling efficiencies up to 95% are possible.

4.2 Study With Antireflection Coatings:

In this section we present the idea of studying with antireflection coatings applied to optical surfaces in order to modify their reflectance/transmittance properties. About 4% of visible light is reflected at any uncoated air-to-glass surface of a lens, prism, or other optical component. For designs using more than a few components, losses in light level can accumulate rapidly. More important are the corresponding losses in image contrast or modulation due to weak reflected "ghost" images superimposed on the desired image. Such unwanted images are often defocused beyond recognition so that contrast reduction (rather than confusion) is their primary effect.

We are able to apply coatings designed to operate within a wavelength region from 200 to 1600 nm. Coating types include single layer dielectrics, multilayer dielectrics and hybrids. Some coatings are for use at a specific wavelength while others cover a broad spectral range.

4.2.1 Single Layer Coatings:

Surface reflectance depends on the difference in refractive indices for air and glass. For visible light this is approximately the difference between 1.0 and 1.5. By selecting a material with an index of refraction that falls between these two values (near the geometric mean), and applying a coating of approximately 1/4 -wavelength optical thickness to the surface, it is possible to reduce the reflectance significantly. Magnesium fluoride (M_gF_2), a durable substance with a thin film refractive index of 1.38 at 550 nanometers, is the most commonly used coating material for single-layer antireflection (AR) coatings.

Instead of one reflection at the air-glass interface, there is a first reflection at the air-M_gF_2 interface followed by a second reflection at the M_gF_2-glass interface. These reflections interfere destructively, resulting in a minimum reflectance within the visible spectrum at normal incidence of 1.5% or less, as compared with with the original 4% for the uncoated glass surface. From the principle of energy conservation, confirmed experimentally, there must be a corresponding increase in overall transmission of a coated surface, including both interfaces.

Such coatings work extremely well over a wide range of wavelengths and angles of incidence., despite the fact that the theoretical idea of zero reflectance is achieved by a film of

1/4-wavelength optical thickness only for normal incidence, and only if the refractive index of the coating material is exactly the geometric mean. In fact, the single layer 1/4-wave thickness M_gF_2 coating designed for normal incidence makes its most significant contribution to the transmission of steep surfaces, where most rays are incident at very large angles.

4.2.2 Multilayer Coatings:

By combining multi-layers of high, medium and low index materials it is possible to cause the reflected and transmitted beams to combine selectively in order to achieve an important performance over a single layer coating. The improvement can be in broadening the spectral bandwidth of the coating or in almost nullifying the reflectance at a particular wavelength.

The typical High Efficiency BroadBand AntiReflection (HEBBAR) coatings give a very low reflectance over a broad spectral bandwidth. The normal (0°) coating typically gives less than 0.5% reflectance over a range of 440 to 660 nm. This coatings can be modified for use at 45° or can be shifted to cover a wavelength range from 750 to 1100 nm.

To obtain the ultimate in transmittance at a single wavelength, it is possible to deposit a "V-coat" which will reduce the reflectance to less than 0.25%, and typically closer to 0.1% for that one wavelength at normal incidence only.

4.3 Mismatching Study:

When power is coupled from the source into the fiber or from fiber to fiber, the center of the emitting area of the source or of the transmitting fiber should be located on the axis along the receiving fiber length to get the maximum coupling efficiency. We have studied the effect of mismatching between the source and the receiving fiber by shifting the source laterally; and calculated the coupling efficiencies for only two specific cases. One can extend this idea to study the effect of mismatching on the coupling efficiency by giving lateral and angular displacements to the source or the emitting fiber for both the source-fiber and fiber-fiber coupling problems. This study may be very useful for designing the transmitter packages, splice and connectors, respectively.

4.4 Remarks:

In this chapter we have presented only some elementary ideas about the further scope of works. These studies may be very useful for the optimum design of the optical systems. These ideas can also be applied to the different type of fibers with different kind of refractive index distributions.

Chapter 5

Conclusions

The main purpose of this thesis is to visualize the optical field characteristics in transmitter packages. In this regard we have studied three different coupling attachment schemes named model-1, model-2 and model-3. We have also studied the the coupling efficiencies for these three coupling arrangements. Finally, we have studied the misalignment problem for model-3 only. In this case the source is shifted laterally in the upward and down-ward directions; and we have studied the effect of the coupling efficiency and the field patterns for this type of simple misalignment problem. The whole results are given as follows.

• We have studied the FD–TD method and Mur's second order absorbing boundary condition. We have presented the results for a point source problem to find the accuracy of the FD–TD method. The computed result is compared with the theoretical result (which is also obtained by a more accurate numerical method; i.e Simpson's rule; for the point source problem), and we have got an error of maximum 15%. Average dielectric constant is taken for the boundary nodes and $\delta y = \delta z = \lambda/10$ is considered to implement the FD–TD method. The FD–TD method is implemented only in two dimensional configurations (i.e. in y–z plane).

• In model-1 we have studied the optical field patterns within the source-fiber region and the coupling efficiency for a flat fiber end face centered directly over the source. We have presented the reflection characteristics of the optical field from the fiber end face by the contour plot. The fundamental field profiles are also given. The coupling efficiency obtained in this case is 38.5027%.

• A taper-end fiber is used in model-2 instead of the flat fiber end face. In this case we have presented the field characteristics by a contour plot. The propagation of the electric field from the source towards the fiber is shown in this contour plot. The reflection characteristics of the

field from the fiber end is also shown in this plot. We have presented the fundamental field profiles within the fiber for this model. Finally, we have calculated the coupling efficiency. The coupling efficiency for this model is 51.937%.

• An efficient coupling arrangement is studied in model-3 by placing a microsphere lens in between the source and the fiber. In this case we have presented the reflection of the electric field from the lens material and the fiber by a contour plot. From this plot we have seen that a strongfield is propagated through the lens and propagates into the fiber. The fundamental field profile within the fiber is also shown for this model. In this case the coupling efficiency is 69.394%. Finally, we have studied the misalignment problem for this model by shifting the source the source laterally in the upward and downward directions. The effect on the reflection characteristics of the field is shown by another contour plot. It is also seen that due to this misalignment the coupling efficiency is reduced to a significant amount.

We have studied these problems by the FD–TD method in two dimensional configurations. The fiber is assumed as a slab waveguide. We have developed the required soft-ware in FORTRAN 77 computer programming language. The main difficulties for the FD–TD method is the requirement of large amount of computer memory and computation time. To study each model the approximate execution time is 25 hours in DEC–ALPHA machine at IIT Kanpur.

Bibliography

[1] K. S. Yee, "Numerical solution of initial boundary value problems involving Maxwell's equations in isotropic media," *IEEE Trans. Antennas Propagat.*, vol. AP-14, pp. 302-307, May 1966.

[2] A. Taflove and K. R. Umashankar, "The finite difference time domain (FD–TD) method for electromagnetic scattering and interaction problems," *J. Electromagn. Waves Appl.*, 1 (4): pp.363-387, 1987.

[3] A. Taflove and K. R. Umashankar, "The finete difference time domain method for numerical modeling of electromagnetic wave interactions with arbitrary structures," in PIER— *Finite Element and Finite Difference Methods in Electromagnetic Scattering*(M. A. Morgan, Ed.) New York: Elsevier, 1990, Ch. 8, pp. 287-373.

[4] A. Taflove and M. E. Brodwin, "Numerical solution of steady-state electromagnetic scattering problems using the time-dependent Maxwell's equations," *IEEE Trans. Microwave Theory Tech.*, vol. MTT-23, pp. 623-630, Aug. 1975.

[5] G. Mur, "Absorbing boundary conditions for the finite-difference approximation of the time-domain electromagnetic field equations," *IEEE Trans. Electromagn. Compat.*, vol. 23, pp. 377-382, Nov. 1981.

[6] P. A. Tirkas, C. A. Balanis and R. A. Renaut, "Higher order absorbing boundary conditions for the finite-difference time-domain method," *IEEE Trans. Antennas Propagat.*, vol. 40, no. 10, Oct. 1992.

[7] K. K. Mei and J. Fang, "Superabsorption—A method to improve absorbing boundary conditions," *IEEE Trans. Antennas Propagat.*, vol. 40, no. 9, Sep. 1992.

[8] J. Fang and K. K. Mei, "A super-absorbing boundary algorithm for solving electromagnetic problems by time-domain finite-difference method," in *Proc. 1988 IEEE Antennas Propagat. Soc. Int. Symp. Syracuse*, New York, pp. 472-475, June 6-10, 1988.

[9] L. N. Trefethen and L. Halpern, "Well-posedness of one-way wave equations and absorbing boundary conditions," *Math. Comp.*, vol. 47, pp. 421-435, Oct. 1986.

[10] J. D. Achenbach, *Wave Propagation in Elastics Solids*, Amsterdam, The Netherlands: North-Holand, 1973, ch. 3, p.94

[11] X. Zhang and K. K. Mei, "Time-domain finite difference approach to the calculation of the frequency-dependent characteristics of micostrip discontinuities, "*IEEE Trans. Microwave Theory Tech.*, vol. 36, no. 12, pp. 1775-1787, Dec. 1988.

[12] S. M. Rao and T. K. Sarkar, "A novel technique to the solution of transient electromagnetic scattering from thin wires," *IEEE Trans. Antennas Propagat.*, vol. AP-34, pp. 630-634, May 1986.

[13] R. F. Harrington, Field Computation by Moment Methods, New York: The Macmillan Company, 1968.

[14] E. K. Miller and A. J. Proggio, "Moment method techniques in electromagnetics from an application viewpoint," Electromagnetic Scattering (P. L. E. Uslenghi, Ed.), Academic Press, pp. 315-157, 1978.

[15] W. J. H. Hoefer, "The transmission line matrix method—theory and application," *IEEE trans. Microwave Theory Tech.*, vol. MTT-33, pp. 882-893, Oct. 1985.

[16] D. T. Moore, "Theory for gradient-index imaging," *Applied Optics*, vol. 19, no. 7-12, pp. 1039-1043, 1980.

[17] K. Kikuchi, S. Ishihara, H. Shimizu and J. Shimada, "Design of gradient-index spherical lenses for optical pickup systems," *Applied Optics*, vol. 19, no. 7-12, pp. 1076-1080, 1980.

[18] W. J. Tomlinson, "Applications of GRIN-rod lenses in optical fiber communication systems," *Applied Optics*, vol. 19, no. 7-12, pp. 1127-1104, 1980.

[19] J. C. Palais, "Fiber coupling using graded-index rod lenses," *Applied Optics*, vol. 19, no. 7-12, pp. 2011-2018, 1980.

[20] A. Nicia, "Lens coupling in fiber-optic devices: efficiency limits," *Applied Optics*, vol. 20, no. 17-20, pp. 3136-3145, 1981.

[21] H. Kuwahara, M. Sasaki and N. Tokoyo, "Efficient coupling from semiconductor laser into single mode fibers with tapered hemispherical ends," *Applied Optics*, vol. 19, no. 13-18, pp. 2453-2456, 1980.

[22] B. S. Kawasaki and D. C. Johnson, "Bulb-ended fiber coupling to LED sources," *Opt. Quantum Electron.*, vol. 7, pp. 281-288, 1975.

[23] J. G. Ackenhusen, "Microlenses to improve LED-to-optical fiber coupling and alignment tolerance," Applied Optics, vol. 18, pp. 3694-3699, Nov. 1979.

[24] R. W. Abram, R. W. Allen and R. C. Goodfellow, "The coupling of light-emitting diodes to optical fibers using sphere lenses," *J. Appl. Phys.*, vol. 46, pp. 3468-3474, Aug. 1975.

[25] O. Hasegawa, R. Namazu, M. Abe and Y. Toyoma, "Coupling of spherical-surfaced LED and spherical-ended fiber," J. Appl. Phys., vol. 51, pp. 30-36, Jan. 1980.

[26] G. K. Khoe and G. Küyt, "Realistic efficiency of coupling light from GaAs laser diodes into parabolic-index optical fibers," *Electron. Lett.*, vol. 16, pp. 667-669, Sept. 28, 1978.

[27] A. Ghatak and K. Thyagarajan, Optical Electronics, Cambridge University Press.

[28] H. G. Unger, Planner Optical Waveguides and Fibers, Clarendon, Oxford, 1977.

[29] G. Keiser, Optical Fiber Communications, McGRAW-HILL BOOK COMPANY, International Student Edition.

Approximate $\left(\frac{\partial H_y}{\partial z}\right)_1$ and $\left(\frac{\partial H_y}{\partial z}\right)_2$ can be given as

$$\left(\frac{\partial H_y}{\partial z}\right)_1 \approx \frac{H_y(m) - H_y(m - \frac{1}{2})}{\frac{\delta z}{2}} \tag{A.6}$$

$$\left(\frac{\partial H_y}{\partial z}\right)_2 \approx \frac{H_y(m + \frac{1}{2})}{\frac{\delta z}{2}} \tag{A.7}$$

where m is assumed to be the position of the interface, and $m + \frac{1}{2}$ and $m - \frac{1}{2}$ denote the positions a half step above and below the interface, respectively.

Substituting (A.6) and (A.7) into (A.4) and (A.5), we get

$$
\begin{aligned}
H_y(m) &\approx \frac{\epsilon_1}{\epsilon_1 + \epsilon_2} H_y\left(m + \frac{1}{2}\right) \\
&+ \frac{\epsilon_2}{\epsilon_1 + \epsilon_2} H_y\left(m - \frac{1}{2}\right) + \frac{\epsilon_2 - \epsilon_1}{\epsilon_1 + \epsilon_2} \frac{\partial H_z}{\partial y} \frac{\delta z}{2}
\end{aligned}
\tag{A.8}
$$

Substituting the $H_y(m)$ value of (A.8) back into (A.6) and (A.7), substituting the resulting (A.6) and (A.7) into (A.4) and (A.5), and adding together, we get

$$
\begin{aligned}
\frac{\epsilon_1 + \epsilon_2}{2} \frac{\partial E_x}{\partial t} &= \frac{\partial H_z}{\partial y} - \frac{H_y(m + \frac{1}{2}) - H_y(m - \frac{1}{2})}{\delta z} \\
&= \frac{\partial H_z}{\partial y} - \frac{\Delta H_y}{\Delta z}
\end{aligned}
\tag{A.9}
$$

Comparing (A.2) and (A.9) we can conclude that for the points at the interface between two media, the effective dielectric constant should be taken as the average of the dielectrics of the media. Similarly, it can be proved that, this averaging rule is also applicable for more than two media.

Appendix B

TE Modes Of A Symmetric Step Index Planar Waveguide

Now we carry out a brief modal analysis of a symmetric step index planar waveguide. We consider only TE mode with E_x, H_y and H_z components ; other components are assumed to be zero. If we choose the z-axis along the direction of propagation, then without any loss of generality, we can write the components in the form of

$$E_x = E_{0x}(y) \, \exp[j(\omega t - \beta z)] \tag{B.1}$$

$$H_y = H_{0y}(y) \, \exp[j(\omega t - \beta z)] \tag{B.2}$$

$$H_z = H_{0z}(y) \, \exp[j(\omega t - \beta z)] \tag{B.3}$$

where we have assumed that field does vary in the x-direction; $E_{0x}(y)$, $H_{0y}(y)$ and $H_{0z}(y)$ are the arbitrary field profiles which depend only on y; and β is the propagation constant. Now from Maxwell's equations we have

$$H_y = \frac{\beta}{\mu_0 \, \omega} E_x \tag{B.4}$$

$$H_z = -\frac{j}{\mu_0 \, \omega} \frac{\partial E_x}{\partial y} \tag{B.5}$$

$$j\epsilon_0 \, n^2(y) E_x = j \, \beta \, H_y + \frac{\partial H_z}{\partial y} \tag{B.6}$$
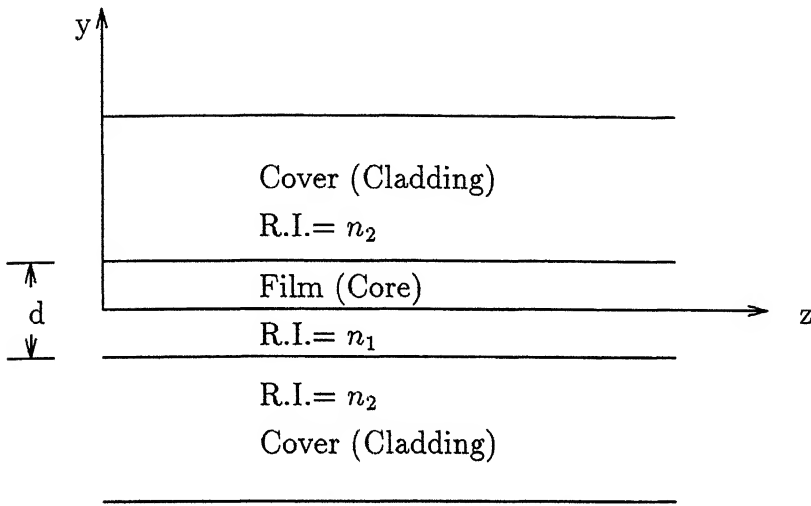
where $n^2(y)$ is refractive index distribution which is assumed to be independent of x and z. Substituting (B.4) and (B.5) in (B.6) we get the following key equation

$$\frac{d^2 E_x}{d \, y^2} + [k_0^2 \, n^2(y) - \beta^2] \, E_x = 0 \tag{B.7}$$
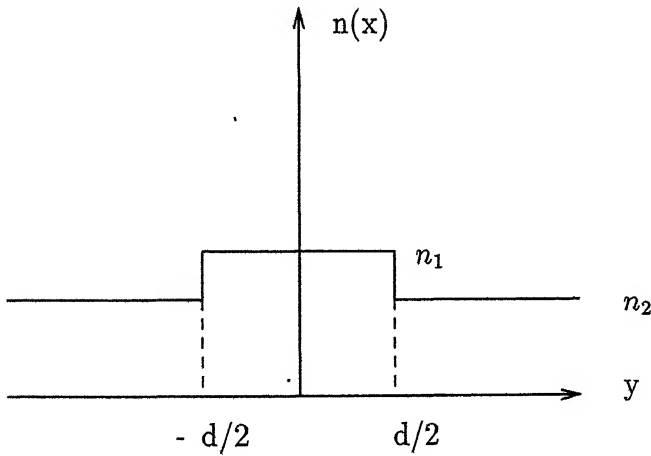
where

$$k_0 = \omega\sqrt{\epsilon_0\,\mu_0}$$

$$= \frac{\omega}{c_0} \tag{B.8}$$

is the free space wave number and $c_0(= \frac{1}{\sqrt{\epsilon_0\,\mu_0}})$ is the speed of light in free space.

(a)

(b)

Figure B.1: (a) The simplest planar optical waveguide (b) The refractive index distribution for a symmetric planar waveguide.

Our analysis is valid for an arbitrary y dependent profile. We now assume a specific field

profile given by (see Figure B.1)

$$n(y) = \begin{cases} n_1; & |y| < d/2 \\ n_2; & |y| > d/2 \end{cases} \tag{B.9}$$

where n_1 and n_2 are the refractive indeces of the core and cladding, respectively and d is the width of the core. To solve the eqn. (B.7) the boundary conditions must be satisfied at the discontinueties. The boundary conditions can be stated as: E_x, H_z and $\frac{dE_x}{dy}$ must be continueous at $x = \pm d/2$. Substituting for $n(y)$ in eqn. (B.7) we get

$$\frac{d^2 E_x}{dy^2} + (k_0^2\, n_1^2 - \beta^2)\, E_x = 0; \quad |y| < d/2 \text{ film} \tag{B.10}$$

$$\frac{d^2 E_x}{dy^2} + (k_0^2\, n_2^2 - \beta^2)\, E_x = 0; \quad |y| > d/2 \text{ cover} \tag{B.11}$$

For guided modes it requires that the field should decay in the cover (in the region $y > d/2$) and thus we must have

$$\beta^2 > k_0^2\, n_2^2 \tag{B.12}$$

Furthermore, to satisfy the boundary conditions at $y = \pm d/2$, we must have also

$$\beta^2 < k_0^2\, n_1^2 \tag{B.13}$$

That is why for guided modes we must have

$$k_0^2\, n_2^2 < \beta^2 < k_0^2\, n_1^2 \tag{B.14}$$

Therefore we can write the eqns.(B.10) and (B.11) in the form

$$\frac{d^2 E_x}{dy^2} + \kappa^2 E_x = 0; \quad |y| < d/2 \text{ film} \tag{B.15}$$

$$\frac{d^2 E_x}{dy^2} + \gamma^2 E_y = 0; \quad |y| > d/2 \text{ cover} \tag{B.16}$$

where

$$\kappa^2 = k_0^2\, n_1^2 - \beta^2 \tag{B.17}$$

and

$$\gamma^2 = \beta^2 - k_0^2\, n_2^2 \tag{B.18}$$

The solution of eqn.(B.15) can be given in the form

$$E_x(y) = A \cos(y) + B \sin(\kappa\, y); \quad \text{for } |y| < d/2 \qquad (B.19)$$

where A and B are constants. The solution of the eqn. (B.16) can be given in the form

$$E_x(y) = \begin{cases} C\, e^{\gamma\, y}; & y < -d/2 \\ D\, e^{-\gamma\, y}; & y > d/2 \end{cases} \qquad (B.20)$$

where C and D are also some constants. A, B, C and D are determined from the boundary conditions. Now if we assume that the refractive index distribution is symmtric about $y = 0$, i.e.

$$n^2(-x) = n^2(x) \qquad (B.21)$$

then the solutions are either symmetric or antisymmetricfunctions of y; thus we must have

$$E_x(y) = E_x(y) \quad \text{symmetricmodes} \qquad (B.22)$$

$$E_x(y) = E_x(y) \quad \text{antisymmetricmodes} \qquad (B.23)$$

For the symmetric mode we must have

$$E_x(y) = \begin{cases} A \cos(\kappa\, y); & |y| < d/2 \\ Ce^{-\gamma\, |y|}; & |y| > d/2 \end{cases} \qquad (B.24)$$

Using the continuity of $E_x(y)$ and $\frac{dE_x}{dy}$ at $x = \pm d/2$ we have

$$A \cos(\kappa\, d/2) = C\, e^{-\gamma\, d/2} \qquad (B.25)$$

and

$$-\kappa\, A \sin(\kappa\, d/2) = -\gamma\, C\, e^{-\gamma\, d/2} \qquad (B.26)$$

respectively. From (B.25) and (B.26) we get

$$(\kappa\, d/2) \tan(\kappa\, d/2) = (\gamma\, d/2) \qquad (B.27)$$

Since

$$\gamma^2 = \beta^2 - k_0^2\, n_2^2$$
$$= k_0^2(n_1^2 - n_2^2) - \kappa^2 \qquad (B.28)$$

we can write

$$\gamma \, d/2 \;=\; \sqrt{(V^2/4 - \xi^2)} \qquad\qquad (B.29)$$

where

$$\xi \;=\; \kappa \, d/2 \;=\; \sqrt{(k_0^2 \, n_1^2 - \beta^2)} \, d/2 \qquad\qquad (B.30)$$

and

$$V \;=\; k_0 \, d \, \sqrt{(n_1^2 - n_2^2)} \qquad\qquad (B.31)$$

is known as the dimensionless waveguide parameter. Therefore (B.27) can be written as

$$\xi \tan \xi \;=\; \sqrt{(V^2/4 - \xi^2)} \qquad\qquad (B.32)$$

Similarly, for the antisymmetric mode we have

$$E_x(y) \;=\; \begin{cases} B \sin(\kappa \, y); & |y| < d/2 \\ \frac{y}{|y|} D \, e^{-\gamma \, |y|}; & |y| > d/2 \end{cases} \qquad\qquad (B.33)$$

and

$$-\xi \cot \xi \;=\; \sqrt{V^2/4 - \xi^2} \qquad\qquad (B.34)$$

Eqns. (B.32) and (B.34) are very useful equations to calculate the propagation constant β of the modes. First, for a particular value of V (B.32 for symmetric mode) or (B.34 for antisymmetric mode) is calculated numerically to obtain the value of ξ. Then β is calculated using (B.30). For example, if $n_1 = 1.5$, $n_2 = 1.499$ and $d = 8.4 \mu m$ from eqn. (B.31) we get $V = 1.927661$. Then using eqn. (B.32) and the Newton-Raphson as the numerical method we get $\xi = 0.722805$ (for symmetric mode). Finally, from eqn. (B.30) we calculate $\beta = 6.283357 \times 10^6$. $\gamma = 0.1518075 \times 10^6$ and $\kappa = 1.720964 \times 10^5$ are also calculed from eqns. (B.29) and (B.30), respectively.

Now we give two important points about the modes.

• If $0 < V < \pi$ we have only one discrete (TE) mode of the waveguide and this mode is symmetric in y. For this case the waveguide is called to be a *single moded waveguide*. For example, if $\lambda = 1.5 \mu m$, $n_1 = 1.5$ and $n_2 = 1.499$ then for a single mode operation we must have (from eqn. (B.31)

$$d < \frac{\pi}{k_0 \sqrt{(n_1^2 - n_2^2)}}$$

. Solving we get

$$d < 13.3 \mu m$$

.

• In general, if

$$2\,m\,\pi < \ V \ < (2\,m+1)\pi$$

there will be $(m+1)$ symmetric modes, and m antisymmetric modes and if

$$(2\,m+1)\pi < V < (2\,m+2)\pi$$

then there will be $(m+1)$ symmetric modes, and $(m+1)$ antisymmetric modes where $m = 0, 1, 2, 3, ...$ The total number of modes will be the integer closest to (and greater than) V/π. Therefore, for $n_1 = 1.50$, $n_2 = 1.499$, $\lambda = 1.50 \mu m$ and $d = 8.4 \mu m$, we have $V = 1.927661$ and therefore only one mode (symmetric) exists within the waveguide.

Appendix C

Coupling Efficiency For Butt Coupling

For single mode fiber the fundamental field profile can be approximated to a Gaussian beam with spot size w_f which is given by

$$w_f = a \left(0.65 + \frac{1.619}{V^{1.5}} + \frac{2.879}{V^6} \right) \tag{C.1}$$

where V is a dimension less parameter of the fiber (see Appendix B) and a is the radius of the core. For butt coupling i.e. centering the fiber end face directly over the (laser diode) source, the maximum coupling efficiency can be given by

$$\eta = \frac{4}{\left(\frac{w_0}{w_f} + \frac{w_f}{w_0} \right)^2 \left[1 + \left(\frac{2z}{k_0 \left(w_0^2 + w_f^2 \right)} \right)^2 \right]} \tag{C.2}$$
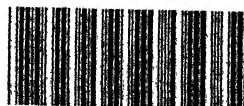
where w_0 is the spot size of the laser beam, z is the distance between the fiber and the source and $k_0 = 2\pi/\lambda$.

For model-1 $V = 1.92$ (see Appendix B), $w_0 = 3.5\mu m$ and $z = 45\mu m$. From equation (C.1) we have $w_f = 5.52727\mu m$. Now using equation (C.2) we can calculate the coupling efficiency for $\lambda = 1.5\mu m$ as $\eta = 0.6523 = 65.23\%$.

Generally, for the butt coupling case coupling efficiency (η) is very less (less than 15%). As w_f approaches to w_0 the coupling efficiency is approaches to 100% for $z = 0$. For the practical cases $w_0 \leq 1.0$. But for our model-1 we have considered $w_0 = 3.5\mu m$ which is very high and that is why the coupling efficiency is also very large compared to that obtained by general experiments.

EE-1995-M-JIT-VIS